PHYSICAL REVIEW A VOLUME 49, NUMBER 2 FEBRUARY 1994

Recurrence spectroscopy: Observation and interpretation of large-scale structure in the absorption spectra of atoms in magnetic fields

J. Main,* G. Wiebusch, and K. Welge
Fakultät für Physik, Universität Bielefeld, D-4800 Bielefeld, Federal Republic of Germany

J. Shaw and J. B. Delos
Physics Department, College of William and Mary, Williamsburg, Virginia 23185

(Received 28 January 1993; revised manuscript received 23 June 1993)

Measurements were made of the absorption spectrum of hydrogen atoms to levels near the ionization threshold in a strong magnetic field. Taking advantage of a classical scaling law, we varied the photon energy and the magnetic-field strength simultaneously, and measured absorption versus $B^{-1/3}$ at fixed scaled energy, $\varepsilon=E/(B/B_0)^{2/3}$. The absorption rate has sinusoidal fluctuations which are correlated with closed classical orbits of the electron. Fourier transformation of this signal gives peaks, which we interpret as "recurrence strength," as a function of the classical action of the closed orbit. Closed-orbit theory gives formulas for these recurrence strengths. We find that the formulas are in good agreement with the measurements. As the scaled energy is increased, observed recurrences proliferate, consistent with a change from orderly to chaotic motion of the electron. Bifurcation theory provides organizing principles for understanding this proliferation and for interpreting the data. New "exotic" orbits suddenly appear through saddle-node bifurcations. The "main sequence" of orbits is produced from an orbit parallel to B through a sequence of pitchfork and period-doubling bifurcations. Other recurrences are created by period-tripling and higher-order bifurcations of existing orbits. These bifurcations can have "generic" structure, or sometimes the structures are modified by symmetries of the system. Focusing effects associated with these bifurcations cause some recurrences to be particularly strong.

PACS number(s): 32.60.+i, 32.80.−t, 05.45.+b, 32.70.Cs

Large-scale structures in absorption spectra—structures that involve the collective effect of many individual absorption lines—contain significant physical information about the system. Such structures can now be calculated directly, without first calculating all the individual lines. The Garton-Tomkins oscillations that are found in absorption spectra of atoms in magnetic fields [1] constitute one such large-scale structure, and, as was pointed out by Edmonds, this structure is correlated with a periodic orbit of the electron moving under combined Coulomb and Lorentz forces. Later, improved measurements showed that this structure contains multiple oscillations [2], and this observation stimulated the development of the theoretical interpretation. A "closed-orbit theory" was created to calculate the absorption spectrum [3], and the earlier "periodic-orbit theory" was used to calculate the oscillatory part of the density of states [4].

Soon afterwards [5–8], large-scale structures were identified in absorption spectra of ozone, $H_3{}^+$, acetylene, and C_2H. In every case the structure is correlated with a recurrence in the system—a classical orbit (or a quantum wave packet) that propagates away from and then returns to some initial location. Each recurrence produces a sinusoidal oscillation $A\sin(TE/\hbar+\delta)$ in the absorption rate and the density of states, where T is the recurrence time (or return time of the orbit). Short orbits produce large-scale structures (long wavelengths on the energy axis) and successively longer orbits produce finer structures. Hypothetically, if recurrences up to infinite time could be calculated, and if the sum over all these recurrences were to converge, then the full set of periodic orbits could be used to calculate the full energy spectrum to any level of resolution. Whether or not this proves to be practical, we know that at least the large-scale structures can be calculated from short-time recurrences. Moreover, since all recurrences are necessarily contained in the time propagator $K(q,q';t)$, it follows that the associated sinusoidal oscillations are contained in the energy Green function $G_E(q,q')$, and therefore that such structure will be manifested in all quantum properties of the system.

The development of the scaled-variables technique [9] for measuring the absorption spectrum of an atom in a magnetic field (varying the proton energy and the magnetic field simultaneously to keep the scaled energy fixed) permits us to observe the structures associated with recurrences with unprecedented precision and detail. These observations stimulated theoretical work leading to a new level of interpretation—classical bifurcation theory was used to interpret the multiplication and proliferation of periodic orbits and their associated recurrences [10].

In this paper we present a full report of these measure-

---

*Permanent address: Theoretische Physik I, Ruhr-Universität Bochum, D-4630 Bochum, Germany.

1050-2947/94/49(2)/847(22)/$06.00

ments, and we show how bifurcation theory combined with closed-orbit theory provides organizing principles for interpreting the observations, as well as quantitative methods for computing the effects of recurrences.

I. EXPERIMENTAL METHOD

In the experiment, hydrogen atoms are excited at the center of the magnetic field in a crossed atom/laser-beam arrangement. The experimental setup is shown in Fig. 1. The excitation is performed in two steps by tunable pulsed radiation (pulse length ~16 ns) linearly polarized parallel to the field axis. With the first step at the Lyman-α wavelength around 1216 A [vacuum ultraviolet (vuv) laser beam] the $|1s,m^g=0\rangle$ ground state is excited to the $|2p,m^i=0\rangle$ intermediate state. At the magnetic-field strengths employed ($2\ \mathrm{T}\leq B\leq 6\ \mathrm{T}$) this transition is fully governed by the Paschen-Back effect. From the intermediate state, Balmer spectra with even parity and magnetic quantum number $m^f=0$ are excited with pulsed laser radiation in the ultraviolet (uv laser beam). The beam intersection point is located between two flat, parallel, fine-mesh grid electrodes (8 mm apart) with their surfaces perpendicular to the magnetic-field axis. These electrodes shield electric fields from the excitation region. A third electrode located 30 mm behind the second grid is kept at a high voltage (+25 kV). Highly excited Rydberg atoms are ionized by the electric field between the second and third electrode. The accelerated electrons are monitored by a detector system composed of a scintillator, plastic fiber, and photomultiplier.

On the basis of the scaling property of the Hamiltonian derived in the following section, we have developed and applied the technique of scaled-variable spectroscopy. According to the relations $\varepsilon=E/(B/B_0)^{2/3}$ and $w=2\pi(B_0/B)^{1/3}$, spectra are taken in the (E,B) plane on lines of $\varepsilon=\text{const}$. The magnetic field is varied in fixed steps of w, adjusting simultaneously E (via the uv laser wavelength) such that the scaled energy ε was kept at a given value ε_1. This procedure is repeated successively at other scaled energies ε_2, ε_3, and so on in steps $\Delta\varepsilon=0.05$ or even $\Delta\varepsilon=0.01$. The range from $\varepsilon=-0.5$ to $+0.02$ was thus covered, which includes the transition regime from regular to chaotic classical motion through the ionization limit ($\varepsilon=0$) into the continuum ($\varepsilon>0$).

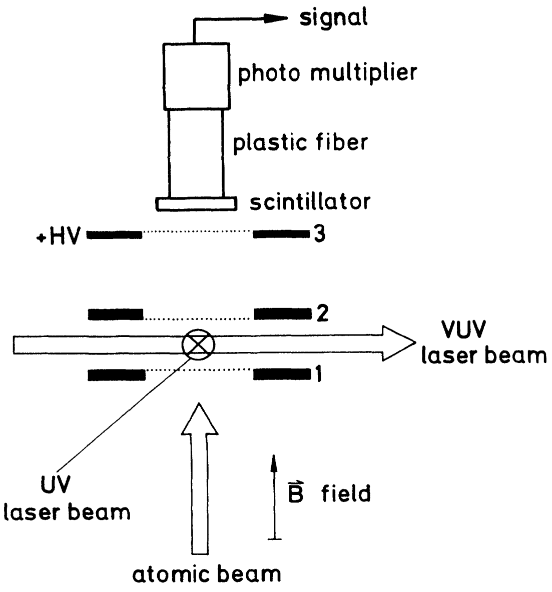

FIG. 1. The experimental arrangement.

The quality of the experimental scaled-variable spectra is determined by the bandwidth of the uv laser ($\delta\nu\approx 1$ GHz) and the absolute accuracy of the varied energy ($\delta E\approx 1\ \mathrm{cm}^{-1}$) and the magnetic-field strength ($\delta B\approx 0.01$ T). From these errors the absolute accuracy of the scaled variables is estimated to be $\delta w\approx 0.25$ and $\delta\varepsilon\approx 0.005$.

II. OSCILLATOR-STRENGTH DENSITY AND ABSORPTION RATE

A. Formulas from closed-orbit theory

The rate of production of atoms in excited states or the rate of ionization, dN/dt, is related to the average oscillator-strength density $\overline{Df}(E,B)$ by the formula

$$\frac{dN}{dt}=\frac{2\pi^2}{c}I_0N_i\frac{\overline{Df}(E,B)}{E-E_i}\ . \tag{1}$$

The average oscillator-strength density can be written as a combination of a smooth background term and a set of sinusoidal oscillations,

$$\overline{Df}(E,B)=Df_0(E)+\sum_n\sum_k g_k C_k^n(E,B)\sin[\Delta_k^n(E,B)]\ . \tag{2}$$

The smooth background term Df_0 is the oscillator-strength density which would exist if there were no magnetic field. Over the energy range considered in this experiment it is practically constant. Each oscillatory term arises from an interference pattern connected with a closed orbit of the electron. Each orbit is labeled by the index k, and the repetitions of each orbit are labeled by n. We call $C_k^n(E,B)$ and $\Delta_k^n(E,B)$, respectively, the "spectral oscillation amplitude and phase," or the "recurrence amplitude and phase." The recurrence amplitude for the nth repetition of the kth classical orbit is given in atomic units by the formula

$$\begin{aligned}C_k^n(E,B)&=(E-E_i)2^{19/4}\pi^{3/2}(\sin\theta_i^k\sin\theta_f^{k,n})^{1/2}\\&\quad\times r_0^{-1/4}A_k^nY(\theta_i^k)Y^*(\theta_f^{k,n})\ ,\\C_0^n(E,B)&=(E-E_i)2^{9/2}\pi r_0^{-1/2}A_0^nY(\theta_i=0)Y^*(\theta_f=0)\ ,\end{aligned} \tag{3}$$

while the phase for that orbit is

$$\begin{aligned}\Delta_k^n(E,B)&=S_k^n-\frac{\pi}{2}\mu_k^n-\frac{3\pi}{4}\ ,\\\Delta_0^n(E,B)&=S_0^n-\frac{\pi}{2}\mu_0^n-\frac{\pi}{2}\ .\end{aligned} \tag{4}$$

The subscript $k=0$ refers to the orbit which is parallel to the direction of the applied magnetic field, $\theta_i=\theta_f=0$. The detailed derivation of Eqs. (2)–(4) is given in Refs. [3] and [11]. We give here only a brief explanation.

The classical orbits are started on an initial spherical surface at the point specified by r_0 and θ_i^k, and the kth orbit returns for the nth time to the initial surface at r_0 with a final angle $\theta_f^{k,n}$. The amplitude of the returning semiclassical wave associated with this orbit, A_k^n, is

$$A_k^n = \left| \frac{d\theta_f^{k,n}}{d\theta_{\text{o}}} \right|^{-1/2}, \quad A_0^n = \left| \frac{d\theta_f^{0,n}}{d\theta_{\text{o}}} \right|^{-1}, \tag{5}$$

where the derivatives are evaluated on the final circle of radius r_{o}. The products $r_{\text{o}}^{-1/4} A_k^n$ and $r_{\text{o}}^{-1/2} A_0^n$ are independent of r_{o} as r_{o} approaches zero. We often call A_k^n the "classical amplitude;" its square is the classical density associated with the family of neighbors of the kth closed orbit [3].

The coefficient g_k is a statistical weight. For every orbit which goes out with $0 \le \theta_i < 90°$, there is another equivalent orbit that goes out with $90° < \theta_i \le 180°$. Therefore all orbits have statistical weight $g_k = 2$, except for the 90° orbit, which has a weight $g_k = 1$. Then the sum in Eq. (2) includes all orbits that begin in the first quadrant.

The phase of the oscillations in the oscillator-strength density is set by $\Delta_k^n(E,B)$, Eq. (4), which contains the classical action of each closed orbit,

$$S_k^n(E,B) = n \oint \mathbf{p} \cdot d\mathbf{q}, \quad S_0^n(E) = n\pi\sqrt{2/-E} \ , \tag{6}$$

where the integral is the action for the first closure of the classical orbit. It is integrated all the way around the trajectory, from $r = 0$ to 0. This integral is simple to evaluate for the parallel orbit. The other contribution to the phase is the Maslov index $\mu_k^n(E,B)$. It is an integer, equal to the number of caustics and foci encountered by the trajectory. The amplitude A_k^n and the Maslov index μ_k^n for the nth return can be calculated from the properties of the orbit on its first return [12].

Finally, the shape of the outgoing wave associated with the kth trajectory is contained in the factors $Y(\theta)$, which contain the dipole operator and the initial-state wave functions [3].

B. Scaled-variable spectroscopy

The Hamiltonian in cylindrical coordinates is

$$H = \frac{1}{2}(p_\rho^2 + p_z^2) - \frac{1}{(\rho^2 + z^2)^{1/2}} + \frac{B^2}{8c^2}\rho^2 \ . \tag{7}$$

The shapes of the classical orbits do not depend on E and B separately, but only on the combination $EB^{-2/3}$ (this combination measures the ratio of the Kepler period to the cyclotron period). Let us define the parameter

$$\gamma = \left[\frac{B}{c} \right] = \frac{[B \text{ (tesla)}]}{2.35 \times 10^5} \tag{8}$$

and defined scaled variables

$$\begin{aligned} \hat{q} &= \frac{q}{2}\gamma^{2/3} \ , \\ \hat{p} &= p\gamma^{-1/3} \ , \\ \hat{t} &= \frac{t}{2}\gamma \ , \end{aligned} \tag{9}$$

$$\begin{aligned} \hat{H} &= H\gamma^{-2/3} \ , \\ \hat{H} &= \frac{1}{2}\left[(\hat{p}_p^2 + \hat{p}_z^2) - \frac{1}{(\hat{\rho}^2 + \hat{z}^2)^{1/2}} + \hat{\rho}^2 \right] . \end{aligned} \tag{10}$$

Since the scaled Hamiltonian contains no parameters, the shapes of the trajectories depend only on the value of the scaled energy,

$$\varepsilon = E\gamma^{-2/3} \ . \tag{11}$$

At any fixed scaled energy, the size and period of each closed orbit still depend on B according to Eqs. (9). We define the scaled action for any orbit to be

$$\hat{S}_k^n(\varepsilon) = \frac{\gamma^{1/3}}{2\pi} S_k^n(E,B) \tag{12}$$

(the factor of $1/\pi$ is an arbitrary convention that was used in Ref. [9]). It follows that at any fixed scaled energy, the action changes with B according to

$$S_k^n(E,B) = \hat{S}_k^n(\varepsilon) w \ , \tag{13}$$

where

$$w = 2\pi\gamma^{-1/3} = 2\pi \left[\frac{c}{B} \right]^{1/3} . \tag{14}$$

Let us now examine the consequences of the above scaling law for the rate of absorption of photons. That rate is a smooth background, $(dN/dt)_{\text{o}}$ related to Df_{o}, plus an oscillatory contribution from each closed orbit. It is convenient to define a reduced absorption rate

$$R(w;\varepsilon) \equiv \frac{c}{2\pi^2 I_{\text{o}} N_i} \gamma^{-1/6} \left[\frac{\overline{dN}}{dt} - \left[\frac{dN}{dt} \right]_{\text{o}} \right] . \tag{15}$$

Applying successively Eqs. (1)–(4) to this expression we find that this reduced absorption rate is given by the formula

$$\begin{aligned} R(w;\varepsilon) &= \gamma^{-1/6} \left[\frac{\overline{dN}}{dt} \right]_{\text{osc}} \frac{c}{2\pi^2 I_{\text{o}} N_i} \\ &= \gamma^{-1/6} \frac{\overline{Df_1}(w;\varepsilon)}{(E - E_i)} \\ &= \sum_n (2\pi)^{1/2} w^{-1/2} D_0^n(\varepsilon) \sin[\Delta_0^n(w;\varepsilon)] \\ &\quad + \sum_n \sum_k D_k^n(\varepsilon) \sin[\Delta_k^n(w;\varepsilon)] \ , \end{aligned} \tag{16}$$

where

$$\begin{aligned} D_k^n(\varepsilon) &\equiv \gamma^{-1/6} g_k \frac{C_k^n(E,B)}{(E - E_i)} \\ &= g_k 2^{19/4} \pi^{3/2} (\sin\hat{\theta}_i^k \sin\hat{\theta}_f^{k,n})^{1/2} \\ &\quad \times [(2\hat{r}_0)^{-1/4} \hat{A}_k^n(\varepsilon)] Y(\hat{\theta}_i^k) Y^*(\hat{\theta}_f^{k,n}) \ , \end{aligned} \tag{17}$$

$$
\begin{aligned}
D_0^n(\varepsilon) &\equiv \gamma^{-1/3} g_0 \frac{C_0^n(E,B)}{(E-E_i)} \\
&= g_0 2^{9/2}\pi[(2\hat{r}_o)^{-1/2}\hat{A}_0^n(\varepsilon)]Y(\hat{\theta}_i=0)Y^*(\hat{\theta}_f=0)\ , \\
\hat{\Delta}_k^n(\varepsilon) &= \hat{S}_k^n(\varepsilon)w - \frac{\pi}{2}\mu_k^n(\varepsilon) - \frac{3\pi}{4}\ , \\
\hat{\Delta}_0^n(\varepsilon) &= \hat{S}_0^n(\varepsilon)w - \frac{\pi}{2}\mu_0^n(\varepsilon) - \frac{\pi}{2}\ .
\end{aligned}
\tag{18}
$$

The phases $\Delta_k^n(w;\varepsilon)$ are linear functions of w; the proportionality constant is the scaled action, $\hat{S}_k^n(\varepsilon)$, which depends on ε but which is independent of w. Similarly the reduced amplitudes $D_k^n(\varepsilon)$ and $D_0^n(\varepsilon)$ are independent of w. To see this, we note that the transformation to scaled variables, Eq. (9), leaves the angles unchanged; therefore the initial and final angles θ_i^k, $\theta_f^{k,n}$ as well as the derivatives $|d\theta_f^{k,n}/d\theta_0|$ are independent of w at fixed ε. Only the boundary radius r_0 must be scaled, and the factors $\gamma^{-1/3}$ and $\gamma^{-1/6}$ in Eqs. (15) and (17) were put into the definitions so that this dependence would be canceled.

It follows from Eq. (16) that at any fixed scaled energy each closed orbit having $\theta_i \neq 0$ contributes to the reduced absorption rate $R(w;\varepsilon)$ a perfectly sinusoidal function of w having fixed wavelength and fixed amplitude. The 0° orbit contributes a sinusoidal oscillation having an amplitude that varies as $w^{-1/2}$ at fixed ε (over the range of the present experiment $w^{-1/2}$ can be replaced by its average value).

The reduced absorption rate $R(w;\varepsilon)$ in Eq. (15) is measurable at fixed ε by varying the photon energy and the magnetic-field strength simultaneously. In Fig. 2 we show an experimental absorption spectrum taken at fixed scaled energy $\varepsilon=-0.23$. The dark line is the same experimental spectrum smoothed by a Gaussian profile. Figure 3 shows the same smoothed experimental spectrum, minus the background, and it shows the theoretical spectrum calculated by including all classical orbits and their repetitions with scaled actions less than $\hat{S}=5$ (about 70 orbits of which 20 dominate). In theory the sum over all orbits and repetitions might reproduce the experimental spectrum to a high level of resolution. The truncated sum ($\hat{S}_k^n \leq 5$) should reproduce the large-scale structure of the spectrum.

The theory gives absolute absorption rates, but the measurement gives relative rates. In Fig. 3 we adjusted the scale of the experimentally measured oscillations so they would be comparable in magnitude to the theoretical ones.

Finally, the arbitrary initial radius r_o or $\hat{r}_o$ can be eliminated from the formulas by making use of semiparabolic coordinates,

$$
\begin{aligned}
&\hat{z} = u^2 - v^2\ , \\
&\frac{d\tau}{d\hat{t}} = \frac{1}{4\hat{r}(\hat{t})}\ , \\
&h = \tfrac{1}{2}(p_u^2 + p_v^2) - 4\varepsilon(u^2+v^2) + 8u^2v^2(u^2+v^2) = 2\ .
\end{aligned}
\tag{19}
$$

These coordinates allow the trajectories to pass through the origin as straight lines. One can show [12] that

$$
\begin{aligned}
r_o^{-1/4} A_k^n &= \gamma^{1/6}(2\hat{r}_o)^{-1/4} A_k^n \\
&= \gamma^{1/6} \left| 2^{3/2} \cos\left(\frac{\theta_i}{2}\right) \cos\left(\frac{\theta_f}{2}\right) J_{12}(k,n) \right|^{-1/2} \\
&= \gamma^{1/6} |2^{-1/2} J_{uv}(k,n)|^{-1/2}
\end{aligned}
\tag{20}
$$

and

$$
\begin{aligned}
r_o^{-1/2} A_0^n &= \gamma^{1/3}(2\hat{r}_o^{-1/2}) A_0^n \\
&= \gamma^{1/3} |2^{3/2} J_{12}(0,n)|^{-1} \\
&= \gamma^{1/3} |2^{-1/2} J_{uv}(0,n)|^{-1}\ ,
\end{aligned}
\tag{21}
$$

where J_{12} is an element of the derivative matrix of the (p_v, v) map,

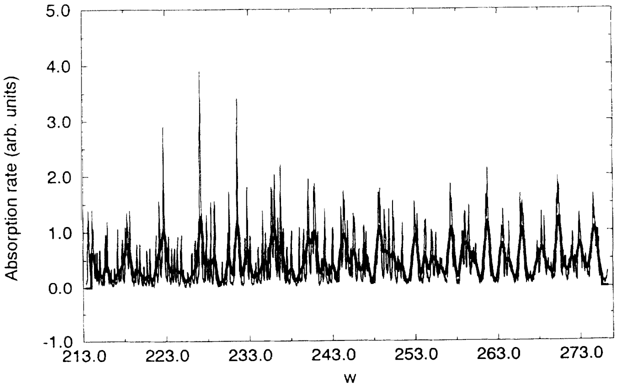

FIG. 2. The absorption rate measured at a constant scaled energy as a function of the field-strength parameter w. The range of the parameter is equivalent to varying the magnetic field from about 6.0 to 2.7 T from the left-hand side of the figure to the right-hand side. The fine line shows the original data from the experiment, while the thick line shows the same experimental data smoothed by a Gaussian profile to emphasize the large-scale structures. The width of the profile was chosen to eliminate structure corresponding to $\hat{S} \gtrsim 5$.

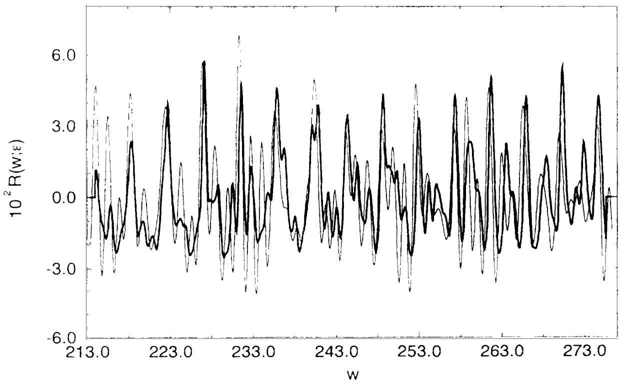

FIG. 3. The thick line is the same smoothed experimental absorption spectrum shown in Fig. 2, and the fine line is the theoretical absorption spectrum calculated by coherently summing the contributions of about 70 closed orbits whose scaled actions are less than or equal to 5. The average background has been subtracted from the experimental spectrum and the magnitude of the oscillations has been scaled to be comparable with the theoretical oscillations.

$$J_{12}=\frac{\partial v_f}{\partial p_{v_i}} \tag{22}$$

and J_{uv} is the semiclassical Jacobian in (u,v) space:

$$J_{uv}=\frac{\partial(u,v)}{\partial(\tau,\Theta_i)}=\frac{\partial(u,v)}{\partial(\tau,\theta_i/2)} \ . \tag{23}$$

Either quantity, J_{12} or J_{uv}, is to be evaluated at the origin $u=0$, $v=0$ on the nth return of the kth closed orbit. Each is smooth near the origin, and has a finite limit as $R=(u^2+v^2)^{1/2}\rightarrow 0$. Formulas analogous to these were first developed by Bogomolnyi [13,12].

C. The Fourier transform of the scaled-variable spectrum

Since $R(w;\varepsilon)$ consists of sinusoidal oscillations, a Fourier transform of the absorption rate with respect to the conjugate variables $\hat{S}$ and w gives peaks at the reduced actions of each orbit. The width of the peaks is set by the range of w (the range of variation of the magnetic field strength at fixed scaled energy).

Let us define

$$\begin{aligned} R(\hat{S};\varepsilon)&\equiv\mathcal{F}R(w;\varepsilon)\\ &\equiv\frac{2}{w_2-w_1}\int_{w_1}^{w_2}e^{-i\hat{S}w}R(w;\varepsilon)dw \ . \end{aligned} \tag{24}$$

From Eq. (16), evaluating the transform and neglecting terms of order $(w_1-w_2)/(w_1+w_2)$, we find

$$\begin{aligned} R(\hat{S};\varepsilon)=\frac{1}{i}\Bigg[&\sum_n\left[\frac{2\pi}{b}\right]^{1/2}D_0^n(\varepsilon)\\ &\times e^{i[bx_0^n-(\pi/2)\mu_0^n-\pi/2]}\frac{\sin[ax_0^n]}{ax_0^n}\\ &+\sum_n\sum_k D_k^n(\varepsilon)e^{i[bx_k^n-(\pi/2)\mu_k^n-3\pi/4]}\\ &\times\frac{\sin[ax_k^n]}{ax_k^n}\Bigg] \ , \end{aligned} \tag{25}$$

where we use the definitions

$$\begin{aligned} x_k^n&=\hat{S}_k^n-\hat{S} \ ,\\ a&=\frac{w_2-w_1}{2} \ ,\\ b&=\frac{w_2+w_1}{2} \ . \end{aligned} \tag{26}$$

In the Fourier-transformed spectrum, each closed orbit produces a peak of the form $\sin(ax_k^n)/x_k^n$ centered at the action of the returning orbit. If there are two or more orbits having nearly equal actions, then the peaks combine coherently—they may add or cancel, depending on the relative phases of the exponential factors in Eq. (25), $\exp i[bx_k^n-(\pi/2)\mu_k^n-\phi_k]$ (with ϕ_k equal to $\pi/2$, $k=0$, or $3\pi/4$, $k\neq 0$).

In a hypothetical ideal experiment, measurements would be carried out over a sufficiently large range of w that all peaks are isolated. In reality we find both well-isolated peaks and overlapping peaks. Observed peaks in the Fourier transform of the measured absorption spectrum may correspond to a single closed orbit, or to a coherent superposition of two, several, or many such orbits.

In Fig. 4(a) we show a needle graph representing the coefficients $[D_k^n(\varepsilon)|^2$ vs $\hat{S}_k^n(\varepsilon)$ for $\varepsilon=-0.23$; these are the weights of the peaks that would arise in the hypothetical ideal experiment [for the $\theta=0$ orbit the relevant coefficient is $|(2\pi/b)^{1/2}D_0^n(\varepsilon)|^2$]. We also show the theoretical transform based on Eq. (25) (actually this is the absolute square of the Fourier transform, the "power spectrum"). We call $D_k^n(\varepsilon)$ and $(2\pi/b)^{1/2}D_0^n(\varepsilon)$ the "scaled recurrence amplitudes," and we call their squares, or $|R(\hat{S};\varepsilon)|^2$, the "recurrence strength."

In Fig. 4(b) the experimental power spectrum is compared to the smoothed theoretical power spectrum. Henceforth we call such graphs "recurrence spectra." The two power spectra agree well except for an underestimate of the amplitude of the coherent sum of the closed

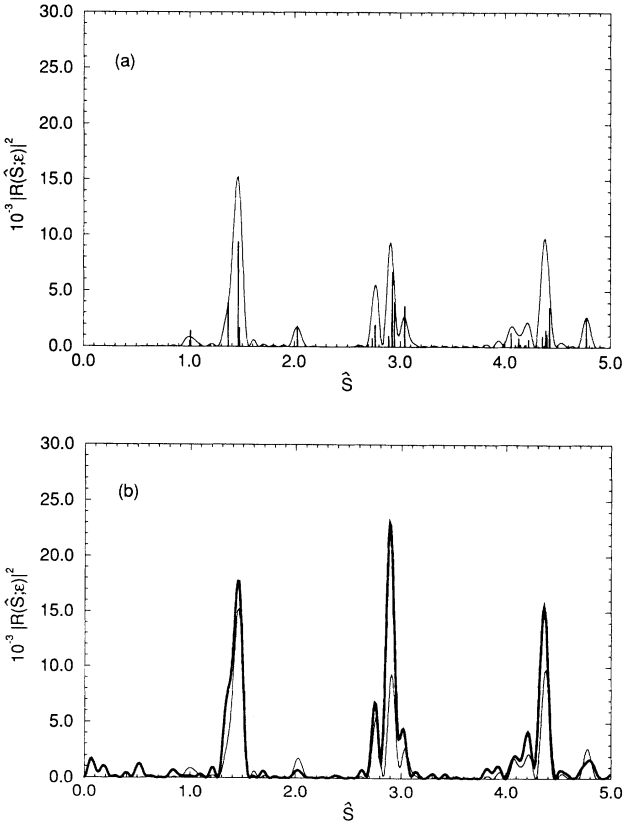

FIG. 4. (a) Needles represent $|D_k^n(\varepsilon)|^2$ or $2\pi/b|D_0^n(\varepsilon)|^2$, the recurrence strengths of individual orbits. The smooth line is the theoretical $|R(\hat{S};\varepsilon)|^2$, Eq. (25). The needles are smoothed and combined to imitate the finite range of the measured Fourier transform. (b) Recurrence strength $|R(\hat{S};\varepsilon)|^2$ at $\varepsilon=-0.23$. Fine line: theory [same as (a)]. Heavy line: experiment.

orbits leading to the large peak near $\hat{S}=3$.

In comparing theory with experiment we take into account the fact that large-action and long-period orbits are somewhat more difficult to detect experimentally than small-action, short-period orbits. The theoretical results are therefore modified by a "cutoff" factor discussed in Appendixes A and B.

III. THEORY CONFRONTS EXPERIMENT

A. The global picture

Measurements of the absorption spectrum were made at 24 different fixed values of scaled energy ε with the magnetic field varied between 6.0 and 2.7 T (corresponding to a range of w from 213 to 277). The resulting Fourier transforms of the measured absorption spectra at each scaled energy are shown as a single graph in Fig. 5. The theoretical recurrence spectra from closed-orbit theory are presented as Fourier transforms in Fig. 6(a) and as needle graphs in Fig. 6(b). The most striking feature of these graphs is the clustering of the peaks of the transformed spectra into distinct groups at low energy, and the proliferation of peaks as the scaled energy increases.

The behavior at low energy is easy to understand. At very low energies ($\varepsilon \lesssim -1$), almost all of the trajectories are regular (multiply periodic). Pictures of such orbits were shown in Figs. 3(a) and 3(b) of Ref. [14]. Each regular orbit can be regarded as a Kepler ellipse with periodically varying orbital parameters, so each such orbit has two fundamental frequencies. One is near to the Kepler frequency, $\Omega_1 \simeq 1/2n^3$, and represents the frequency of the motion of the electron around the ellipse. The other frequency Ω_2 is much lower, and represents the frequency of periodic variation of the orbital parameters. These two frequencies are continuous functions of their conjugate action variables, which are conserved on each trajectory.

The regular orbits form themselves into three families [14]. One family is centered on the ρ axis (rotators), while the other two are centered on the $\pm z$ axes (vibrators). Within each family of multiply periodic orbits, periodic orbits are embedded: whenever the ratio of frequencies Ω_2/Ω_1 is a rational number, i/j, then the orbit

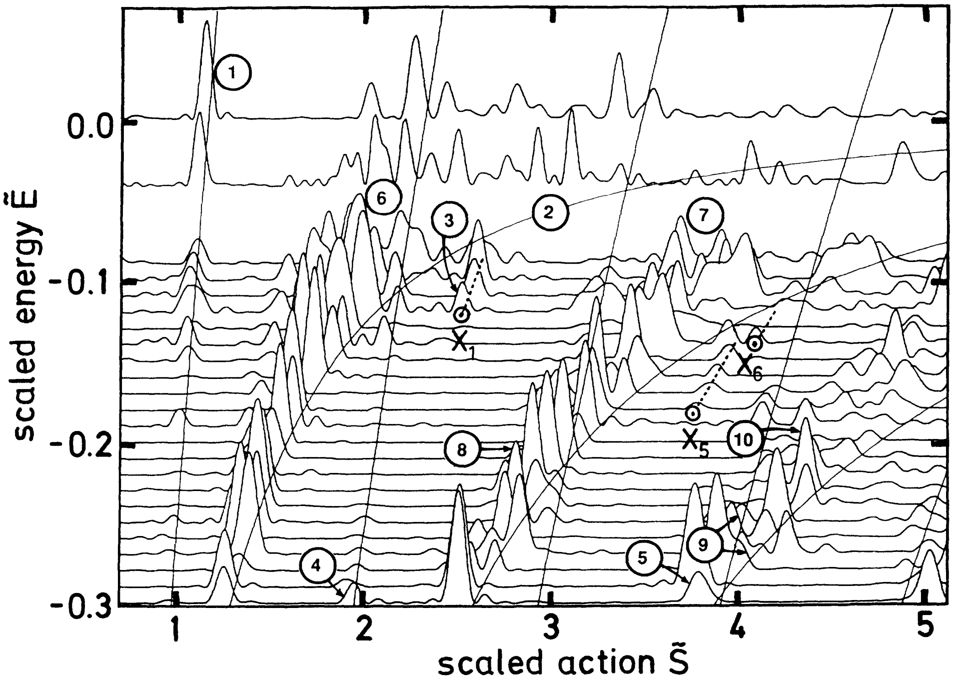

FIG. 5. Experimental |(Fourier transforms)|^2 (recurrence strengths) at each scaled energy are drawn in a single graph. The following structures will be explained. (1) The lowest-action peak results from an orbit that lies perpendicular to the magnetic field. The nearly vertical lines represent the action vs energy for the first return and subsequent returns of this orbit. (2) The curved line represents the action vs energy of the orbit that lies parallel to the magnetic field. (3) A new peak appearing "out of nowhere" is caused by a saddle-node bifurcation that produces an "exotic" orbit (Figs. 7–9). (4) A focusing effect gives a strong recurrence at the second return of the perpendicular orbit and again, (5) at the fourth return (Figs. 11 and 12). (6) The first "mountain range" is produced by the "main sequence" of orbits that bifurcate from the parallel orbit [Figs. 19(a) and 20]. (7) The second mountain range arises from orbits shown in Figs. 19(b), 19(c), and 23. (8) In particular, this large peak arises mainly from the orbit shown in Fig. 19(c1) (see also Fig. 22). (9) The shoulder on this peak arises from the orbit shown in Fig. 19(e2) (see also Fig. 24). Almost hidden behind it is the set of three peaks shown in Fig. 25. Of these peaks, the middle one is produced by a generic period tripling of the balloon orbit B_1 [Fig. 19(a)]. (10) This prominent peak is also shown in Fig. 25. It is produced by a cluster of orbits resulting from period tripling of the first snake orbit S_1 [Fig. 19(a)].

is periodic and has frequency $i\Omega_1 = j\Omega_2$. Most such periods are very long: they are a usually large multiple of $2\pi/\Omega_2$, which itself goes to infinity as ε becomes large and negative.

However, there remain four short-period orbits even at large negative ε: one that moves on the ρ axis, two that move on the $\pm z$ axes, and one that approaches a circle in the ρ-z plane. Of all the orbits that exist at any given scaled energy, the present experiment gives a signal [a peak in $R(\hat{S};\varepsilon)$] for the relatively short orbits that begin and end at the nucleus. Accordingly, we expect a peak at actions corresponding to the orbits on the ρ axis and on the $\pm z$ axis.

At $\varepsilon \simeq -0.3$, the orbit on the ρ axis (the perpendicular orbit) has scaled action $S \simeq 0.975$. A small peak is plainly visible there (actually it is a large peak, but it is small compared to some of the others). Peaks at actions corresponding to subsequent returns of this orbit to the nucleus are also visible in Fig. 5 at $\hat{S} = 1.95$, 2.91 (barely visible at this scale), and at 3.9 (combined with other orbits).

At this value of ε, the orbits on the $\pm z$ axes (the paral-

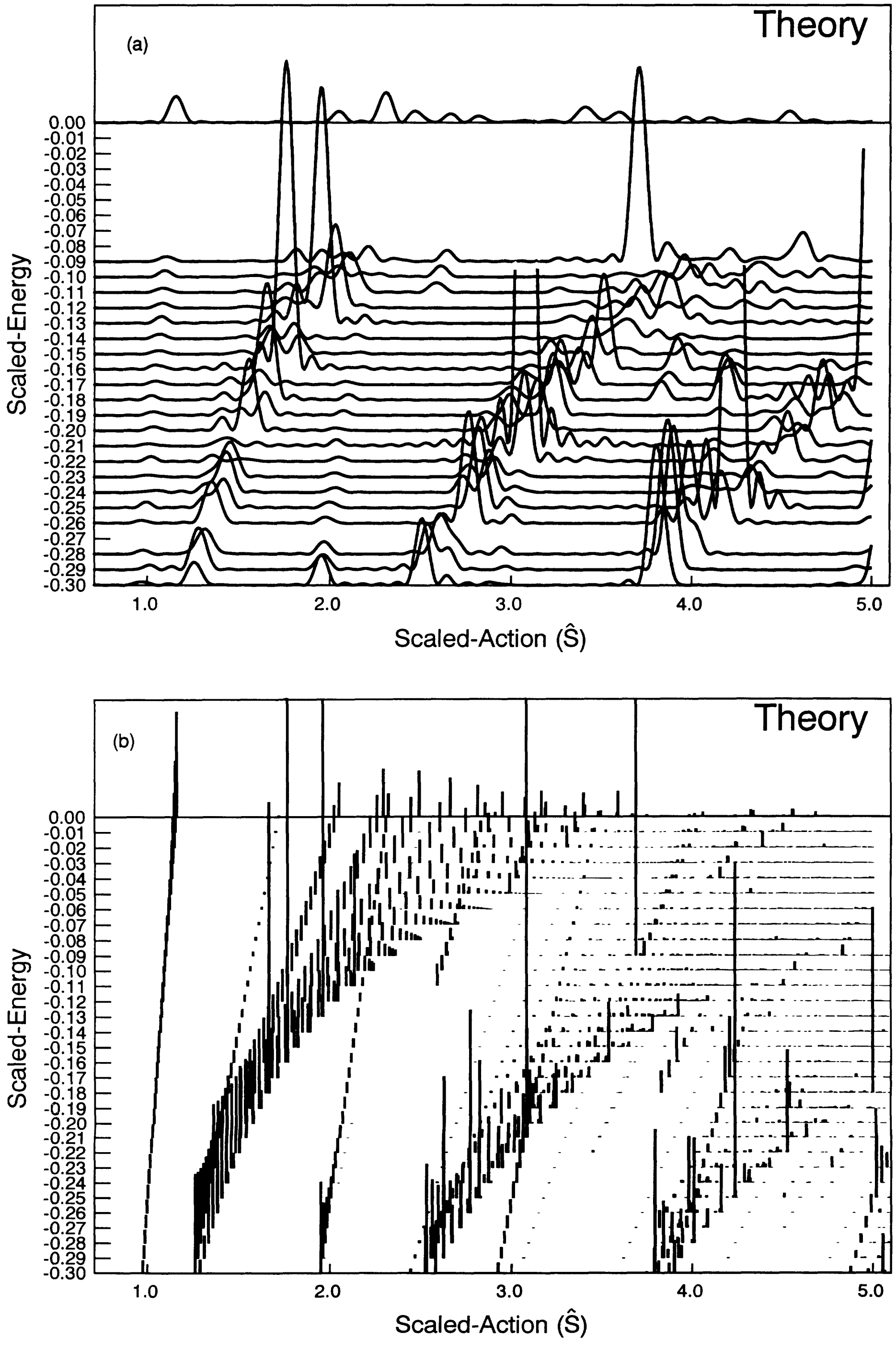

FIG. 6. (a) Theoretical |(Fourier transforms)|^2 (recurrence strengths) at each scaled energy are drawn in a single graph. The transforms are scaled by a linear function of scaled energy so that the peaks at low energies do not obscure the peaks at higher energies. Excessively large peaks from nearly resonant recurrences where the semiclassical amplitude is singular have been arbitrarily cut off. (b) Theoretical recurrence strengths for each scaled energy as a three-dimensional needle graph. For each scaled energy ε a needle is placed at the scaled action of a particular orbit of the electron. The height of each needle is the recurrence strength $|D_k^n(\varepsilon)|^2$. The connection between these classical orbits and the peaks measured and shown in Fig. 5 is clearly visible. All needles are multiplied by the same linear function of scaled energy.

lel orbits) have scaled actions equal to 1.291, and we can see peaks near 1.3, 2.6, and 3.9. However, it turns out that the amplitude $D_k^n(\varepsilon)$ associated with this orbit is quite small, and detectable only at significantly lower values of ε. As we will explain below, the observed peaks result from orbits that bifurcate out of the 0° orbit and have nearly the same action.

As the scaled energy ε is increased, we see that the individual peaks split into mountain ranges. In the underlying classical dynamics order changes to chaos as ε increases. Whereas regular systems have simple, orderly families of closed orbits, chaotic systems possess many closed orbits. General arguments give a rule for the number of periodic orbits of a given length that may appear: in a typical regular system the number of periodic orbits having action less than $S_{\max}$ increases as a power of $S_{\max}$, as $S_{\max}^2$ in our case; however, in a typical chaotic system the number increases exponentially with $S_{\max}$. Therefore, as ε increases and order changes to chaos, periodic orbits must proliferate.

Where do new periodic orbits come from? Some bifurcate out of the parallel and perpendicular orbits; others bifurcate out of these new orbits; still others appear "out of nowhere," in stable-unstable pairs.

A general theory has been developed that describes the types of bifurcations that typically occur in a Hamiltonian system [15]. This theory asserts that typical bifurcations can be classified into five basic families—we call them saddle-node, period-doubling, touch-and-go (two types), and island-chain bifurcations. In our system, as a result of symmetries, the structures of some of the bifurcations are modified, and another type—a pitchfork bifurcation—also appears.

This classification scheme and its application to our system have been described in Ref. [10]. In this paper we show how those various bifurcations manifest themselves in the experimental measurements.

We examine first the saddle-node bifurcations, then bifurcations from the perpendicular orbit, then those from the parallel orbit.

B. Saddle-node bifurcations and exotic orbits

Isolated orbits which do not bifurcate from the parallel or perpendicular orbits (or from their progeny) have been designated "exotics," and have been denoted by $X_1, X_2, X_3, \ldots$. Because they may be born with actions lying in the gaps between the major sequences, the exotics often have clear signatures which can be seen in relative isolation in the experiment.

Each exotic, such as X_1 shown in Fig. 7, is actually a pair of orbits, one stable and one unstable, which appears by saddle-node bifurcation [16]. This one occurs at a scaled energy of $\varepsilon = -0.115\,442\,3$. A surface of section shows the creation of both a stable and an unstable closed orbit at this energy [10]. In general, the Maslov indices of the two orbits must differ by 1; in this case, the Maslov index for the first closure of the initially stable branch is 6, while the Maslov index of the unstable branch is 7. Both branches of X_1 continue to higher energies, and at a scaled energy of $\varepsilon = -0.115\,426\,5$, the stable orbit also goes unstable.

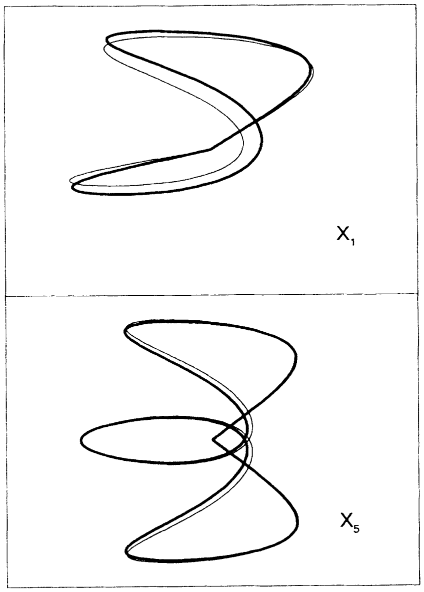

FIG. 7. The clearest example of an "exotic" orbit is the pair of orbits designated as X_1. The heavier line highlights the unstable member of the pair, which lies slightly closer to the z axis than the originally stable member, which is shown in a finer line. Both orbits have nearly the same action and both contribute to the peak seen in the measurements at scaled energy $\varepsilon = -0.11$. Another exotic orbit of interest is the pair of orbits designated X_5. They are symmetric with respect to the $z = 0$ plane unlike the exotic X_1 (this leads to different bifurcation behavior). As before, the originally unstable orbit is the heavy line, the originally stable orbit is the lighter line.

Figure 8 shows the theoretical behavior of the semiclassically calculated amplitudes $A_k^n(\varepsilon)$ for each branch as a function of scaled energy. In our semiclassical formulas, the amplitude $A_k^n(\varepsilon)$ at the bifurcation energy is infinite, and then it decreases as $|\varepsilon - \varepsilon_{\text{bif}}|^{-1/2}$. A full quantum theory of this bifurcation is being developed.

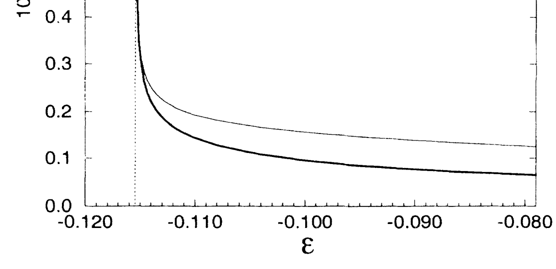

FIG. 8. The amplitudes for both the originally stable and unstable X_1 orbits are shown together as a function of the scaled energy. As before, the thick line is the originally unstable orbit while the thin line is the originally stable orbit.

The quantum theory must give a finite result at all values of ε and we expect that it will also give a small but nonzero amplitude slightly below the bifurcation energy [17].

The appearance of a new peak "out of nowhere" is evident in Fig. 5 at $\varepsilon=-0.12$, $\hat{S}\simeq 2.6$. This is shown in more detail in Fig. 9.

One more interesting aspect of this bifurcation is visible in Fig. 9. In the experimental measurements, a peak seemingly associated with the exotic X_1 is already visible at $\varepsilon=-0.12$, *just below* the bifurcation. We would be delighted to attribute this to a kind of quantum tunneling effect: the new pair of orbits makes itself visible in the quantum system before it manifests itself in the classical system. However, experimental uncertainties in the photon energy and the magnetic-field strength would provide the same effect, so the measurements must be reexamined before this interpretation can be accepted.

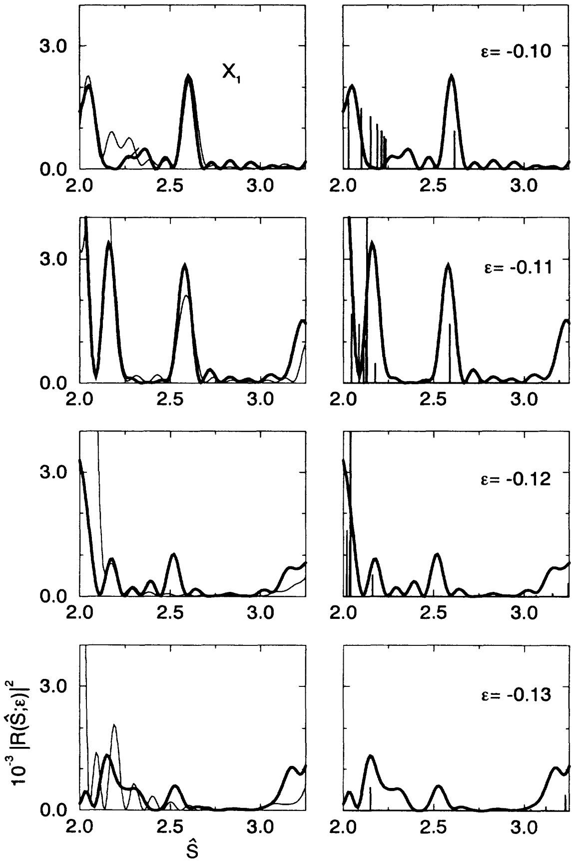

FIG. 9. The saddle-node bifurcation of X_1 in more detail. The four pictures on the right compare the experimental recurrence strengths $|R(\hat{S};\varepsilon)|^2$ with theoretical needle graphs, while those on the left compare the experiment (heavy) with smoothed theoretical curves (light). In the theory the two newly created exotic orbits X_1 produce a new pair of needles or a new peak at $\varepsilon=-0.11$, $\hat{S}\simeq 2.6$. In the experiment at the lowest energy $\varepsilon=-0.13$, there is a small bump, but this is comparable to the "background" hills that appear in all of the measured Fourier transforms. At the higher energies, $\varepsilon=-0.10$ and -0.11, the new large peak is visible. At $\varepsilon=-0.12$, the new peak is present in the experiment before it appears in the theory (see discussion in text).

The exotic X_5, Fig. 7, is also clearly seen in both theory and experiment as a new isolated peak. X_5 is also born as a stable-unstable pair at a scaled energy $\varepsilon=-0.18057$ with scaled action near $\hat{S}=3.85$, Fig. 5.

Many more exotic orbits are found in calculations and indeed many of them can be sorted into orderly sequences. They are all born by saddle-node bifurcations, as stable-unstable pairs. At the bifurcation energy, both the stable and unstable orbits have identical periods and actions, and the periods and actions move apart as the scaled energy increases above the bifurcation point. The classical amplitude for each orbit is infinite at the bifurcation energy, drops rapidly with increasing energy just above the bifurcation, then levels off. The amplitude for either the stable or unstable branch may increase again for some values of the scaled energy far from the original bifurcation (we will show an example later). The amplitudes for the two orbits of a pair are comparable but not equal, as was seen in Fig. 8. In the experimental measurements, a few of these other exotics are visible, but in some cases the peaks are barely above the "noise" level of the experimental transform, and in others the exotics are masked by other peaks nearby.

C. The perpendicular orbit

The first closure of the perpendicular orbit is called R_1, and its subsequent closures are called R_n. R_1 is the dominant feature of the Fourier spectrum at scaled energy equal to zero. It is the orbit with the shortest period and action, both of which vary only slowly over the total range of scaled energy examined. It is one of the two fundamental closed orbits which remain in the low-energy limit, and the oscillations associated with this orbit were the first ones that were seen in the original experiments of Garton and Tomkins ("quasi-Landau oscillations").

Figure 5 seems to show the rapid disappearance of this peak as the energy is lowered. This apparent disappearance of R_1 in the experiment is an artifact of the relative normalizations used to draw Fig. 5. The amplitude of R_1 actually increases slowly with decreasing scaled energy, but there are other much larger peaks in the spectrum at lower scaled energy. Since the experimental Fourier transforms were normalized so that the highest peaks at each scaled energy were of comparable height, the amplitude associated with R_1 was pushed into the background.

This orbit is stable below $\varepsilon=-0.12727$ and unstable above this point. This change of stability produces an interesting effect that is visible in the measurements.

For unstable orbits, the amplitude associated with the nth repetition of the orbit decreases approximately exponentially with increasing n. Precise formulas are given in Ref. [12]. For unstable orbits [18], one can show that

$$A_k^n(\varepsilon)=\left|\frac{\sinh[\beta_1(\varepsilon)]}{\sinh[n\beta_1(\varepsilon)]}\right|^{1/2} A_k^1(\varepsilon)\ , \qquad (27)$$

where β_1 is the stability exponent and A_k^1 is the semiclassical amplitude given by Eq. (5) evaluated on the first closure of the unstable orbit. The formula predicts that the amplitude decreases exponentially with n at a rate proportional to the stability exponent (similar formulas are well known in the Gutzwiller trace theory for the density of states). The amplitudes A_n for R_n at $\varepsilon=0.0$ are shown as a function of action in Fig. 10(a). This is difficult to observe in the present experiment because the peaks are masked by larger peaks associated with other orbits. However, in an earlier experiment,[2] we can see peaks associated with the first three repetitions of the perpendicular orbit plotted against time. The comparison in Ref. [3] showed theory in good agreement with that experiment. The relative amplitudes measured experimentally give an empirical estimate of the stability exponent for R_n at $\varepsilon=0.0$. The estimate from the experiment is $\beta_1 \approx 1.4-1.9$, which is in reasonable agreement with the theoretical value of 1.4.

The amplitudes of repetitions of stable orbits behave in a completely different way. In the present case, one can show that for stable orbits [18] the amplitude associated with the nth return is related to that on the first return by

$$A_k^n(\varepsilon)=\left|\frac{\sin[\alpha_1(\varepsilon)]}{\sin[n\alpha_1(\varepsilon)]}\right|^{1/2} A_k^1(\varepsilon) . \tag{28}$$

Here α_1 is the winding angle of a neighboring trajectory about the central closed orbit [12]. This formula gives what amounts to a quasiperiodic function: it is a periodic function of a continuous variable n having period $\Delta n = 2\pi/\alpha_1(\varepsilon)$, but the function is evaluated at discrete points (integer n) having no relationship to the period. To illustrate this quasiperiodicity Fig. 10(b) shows the amplitude of the first 20 repetitions of R_n at $\varepsilon=-0.2455$.

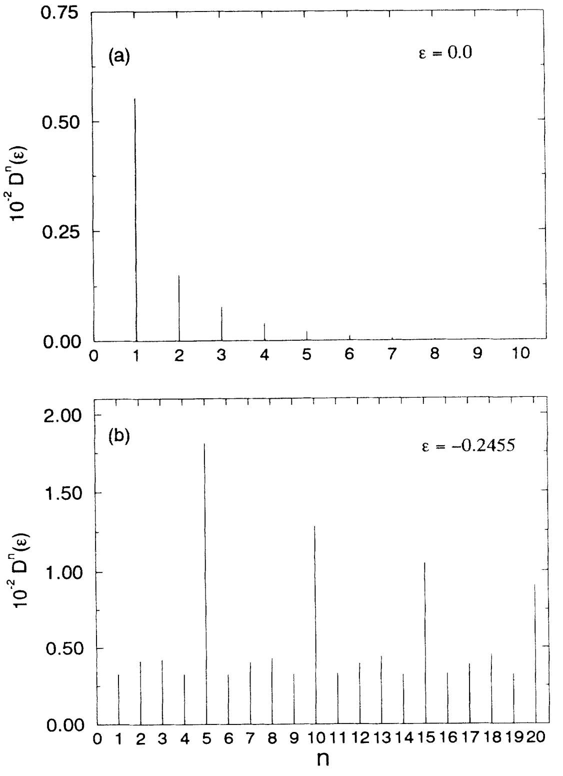

FIG. 10. (a) The amplitude behavior vs repetition number n at fixed scaled energy, $\varepsilon=0.0$, for the perpendicular orbit when it is unstable. (b) The amplitude behavior vs n at fixed scaled energy, $\varepsilon=-0.2455$, for the perpendicular orbit when it is stable and near a 5:2 resonance. The exact energy for the resonance is near $\varepsilon_{\text{crit}}=-0.246206$.

As long as the winding rate $\alpha_1(\varepsilon)$ is an irrational number, the amplitudes $A_k^n(\varepsilon)$ are nonsingular. However, let us now consider what happens as we vary ε. The winding rate varies continuously through rational and irrational numbers. Therefore, if we now fix n and consider A_k^n as a function of energy ε, then for each n there exist critical values of the energy such that

$$n\alpha_1(\varepsilon)=m\pi, \quad m=1,2,\ldots, \quad n>1 . \tag{29}$$

The classical amplitude on the nth return A_k^n is infinite at such points. Physically, this resonance condition implies that the period of stable oscillations transverse to the orbit is commensurable with the period of the orbit itself. As a consequence, the neighbors of the orbit, which begin at the nucleus and move away from the central orbit, all return to the central orbit at the moment that the orbit returns to the nucleus. Therefore a focus exists at the origin on the nth closure of the central trajectory. The derivative $|d\theta_f^n/d\theta_0|$ entering the denominator of Eq. (5) for A_k^n is zero at a focus, so A_k^n diverges. Experiments show that the recurrence amplitude gets large, but remains finite near these resonances. For scaled energies close to such a resonance, the divergent semiclassical amplitude A_k^n is not a valid approximation to the actual observed amplitude for R_n, but it is a good approximation to the observed amplitude at energies sufficiently far away from the resonance.

We can see the effect of such near resonances in the experimental recurrence spectra.

Figure 11 shows the experimental and calculated power spectrum for the scaled energy $\varepsilon=-0.30$. The theoretical calculation showing the R_n orbit alone is

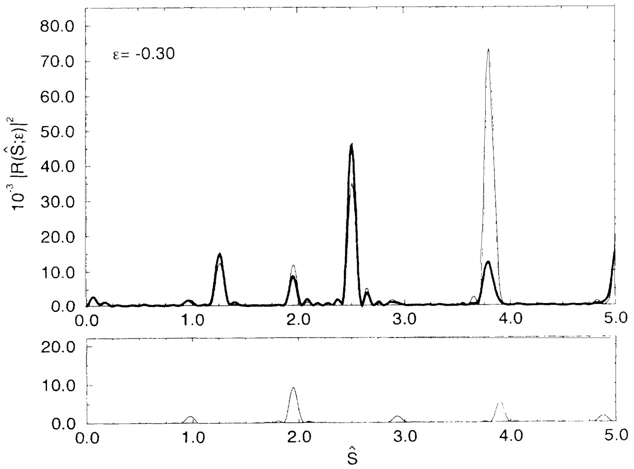

FIG. 11. Upper part: heavy line is the experimental recurrence strength $|R(\hat{S};\varepsilon)|^2$ for $\varepsilon=-0.30$; fine line is the smoothed theoretical result. Lower part: Contribution of the perpendicular orbit and its repetitions. Note the alternation of small and large amplitudes that is also visible in the measurements.

shown in the lower part of the figure. The amplitudes of the $n=2$ and 4 repetitions of R_n are much larger than the $n=1$ and 3 repetitions. These large values for even repetitions are caused by a near-resonance: the perpendicular orbit has a 4:1 resonance at $\varepsilon=-0.316\,19$ [19].

To show the consequences of this resonance in a more intuitive way, we show in Fig. 12 a family of neighbors of the perpendicular orbit at this energy.

On the first closure, shown in Fig. 12(a), the neighboring trajectories are widely spaced and the configuration space density is low. The returning wave [Fig. 12(b)] has a broad wave front, having only a small overlap with the initial quantum state localized at the origin. In Fig. 12(c) the attractive Coulomb field turns the orbits around, and they go back out below the ρ axis. On the second return [Fig. 12(d)], the neighboring trajectories, and the returning wave, converge almost to a focus in the region near the nucleus. This focusing effect gives a large overlap with the initial state [20] (i.e., a strong recurrence), which produces a strong interference effect and large-amplitude oscillations in the spectrum.

If the neighbors converge exactly on the nucleus (which happens at $\varepsilon=-0.316\,19$), then the Coulomb field sends them back exactly the way they came. The outgoing wave then looks like the original outgoing wave, and the orbits turn around and produce a weak signal on the third return (exactly the same as the first return). They turn around again and produce a strong signal on the fourth return. This is precisely what we see in the experiment at $\varepsilon=-0.30$.

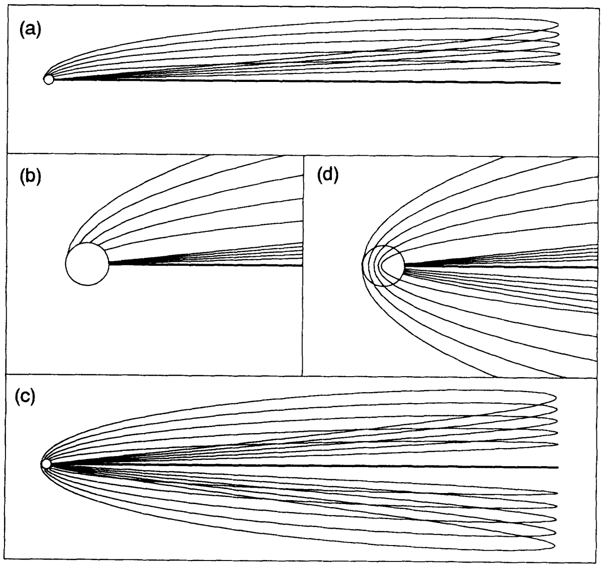

FIG. 12. (a) The outgoing pencil of rays (family of neighbors) of the perpendicular orbit at $\varepsilon=-0.30$. The orbits turn around and carry wave fronts back to the nucleus. The rays are spread over a broad front, and the amplitude of the returning wave is relatively small. The size of the large figure is $\sim 2000a_0$, and the expanded inset (b) is $\sim 20a_0$. (c) The orbits are turned around by the Coulomb field. (d) On their next return they are well focused at the nucleus. Waves return on a narrow front with a large amplitude. At this energy even-numbered returns have a much larger effect than odd-numbered returns.

In Fig. 13 we show the recurrence strength, $R(\hat{S};\varepsilon)$, for the perpendicular orbit as a function of ε for $n=1,2,3$. R_3 has a resonance at $\varepsilon=-0.209\,29$ which is in the range of the experiment. Figure 14 shows theoretical and experimental results over a range of scaled energy bracketing this resonance. The agreement is good except at $\varepsilon=-0.21$. There, the 6:1 resonance in the perpendicular orbit gives an excessively large peak on the third return ($\hat{S}=3.08$).

Such failures of semiclassical approximations near a focus are familiar in optics. In a future publication we plan to repair the formulas to cover such cases.

In optics we also know that a focus produces an additional phase loss of $\pi/2$. In semiclassical approximations this additional phase information is contained in the Maslov index. We find that for the perpendicular orbit, the Maslov index for the nth repetition decreases by one as the scaled energy increases past the critical energies for that repetition.

These resonances are also tied to bifurcations. The resonance visible in the experiment at $\varepsilon=-0.30$ is tied to the creation of a closed orbit of a particular shape (the one we named "PacMan" or R_2^1 in Ref. [10]). The 6:1 resonance at $\varepsilon=-0.21$ also produces new closed orbits ($P_{1.5}\equiv R_3^2$). The complicated sequence of these bifurcations is discussed in Ref. [10].

D. The parallel orbit

The orbit parallel to the direction of the magnetic field has special importance. Although it is only barely visible itself in the experiments, the largest "mountain ranges" in Fig. 5 come from the orbits that bifurcate from it, and the large-action edge of the mountain range represents

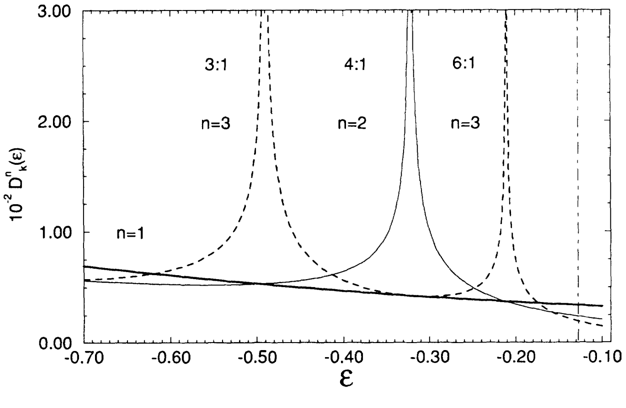

FIG. 13. We show $D_k^n(\varepsilon)$ as a function of ε for each return of the perpendicular orbit. The heavy line, (1), is the amplitude associated with the first return, which shows a slow monotonic decrease in amplitude with increasing scaled energy. The light solid line, (2), is the classical amplitude for the second return. It diverges at $\varepsilon=-0.316\,19$, at the 4:1 resonance discussed in the text. At this point the amplitudes on the first and third returns are equal (to understand why, study Fig. 12). The dashed line shows the amplitude on the third return; it has two resonances, a 6:1 and a 3:1. The 6:1 resonance occurs within the experimental range and causes a failure of the semiclassical approximation at $\varepsilon=-0.21$ (Fig. 14).

the action versus energy of the parallel orbit. In Ref. [9], the parallel orbit was called V_1, and its repetitions were labeled V_n.

1. Organizing principles from bifurcation theory

To make easier the discussion of the parallel orbit and the orbits which bifurcate from it, we need some information from bifurcation theory. A more complete development of this is given in Ref. [10].

We work in scaled semiparabolic coordinates (u,v) and we define a modified Poincaré map such that p_v and v are recorded every time u passes through zero for *either sign* of p_u. We have the mapping

$$\begin{aligned} &\mathbf{z}_1=f(\mathbf{z}_0;\varepsilon)\ , \\ &p_v\equiv p,\quad v\equiv q\ , \\ &\mathbf{z}\equiv(p,q)\ . \end{aligned} \tag{30}$$

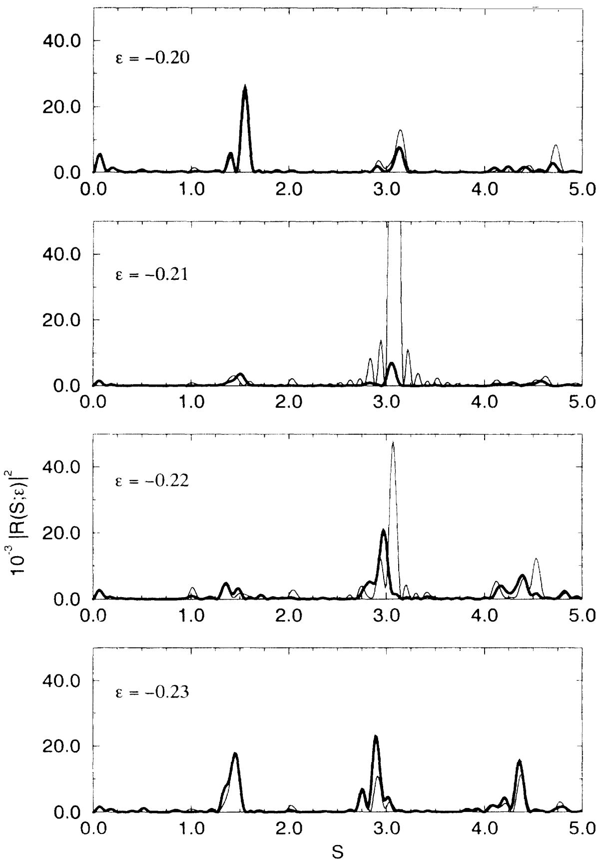

FIG. 14. The effect of a resonance on the agreement between theory and experiment. This figure shows a range of scaled energy bracketing the 6:1 resonance at $\varepsilon=-0.2092$. The scaled-energy measurements were taken in steps of 0.01 in ε in this energy range. At all energies and actions we have good to excellent agreement with the experimental measurements except at $\varepsilon=-0.22$ and -0.21 at the scaled action corresponding to the third return of the perpendicular orbit. The semiclassical amplitude approximation fails here because of the proximity to the resonance. It is clear from the experiment that the true recurrence strengths remain bounded and finite.

Every periodic orbit of this map corresponds to a periodic orbit of the Hamiltonian, Eq. (19). The period of the orbit in uv space either corresponds to exactly the map period (if the map period is even), or it corresponds to twice the map period (if the map period is odd). The Jacobian matrix associated with this mapping [21] is

$$\begin{aligned} \underline{J}_1(\mathbf{z};\varepsilon)&\equiv\begin{bmatrix} \dfrac{\partial q_1(p,q;\varepsilon)}{\partial q} & \dfrac{\partial q_1(p,q;\varepsilon)}{\partial p} \\ \dfrac{\partial p_1(p,q;\varepsilon)}{\partial q} & \dfrac{\partial p_1(p,q;\varepsilon)}{\partial p} \end{bmatrix} \\ &\equiv\begin{bmatrix} J_{11} & J_{12} \\ J_{21} & J_{22} \end{bmatrix} \end{aligned} \tag{31}$$

and the trace of this matrix is

$$\mathrm{Tr}_1\equiv\mathrm{Tr}_1(\mathbf{z};\varepsilon)\equiv\mathrm{Tr}[\underline{J}_1(\mathbf{z};\varepsilon)]\ . \tag{32}$$

The structure of the bifurcations on the Poincaré map is determined by the value of this trace evaluated at the periodic orbit at a map period of the orbit.

If the absolute value of this trace is greater than 2, then the orbit is unstable, and it does not bifurcate. If it is less than 2, the orbit is stable, and it can bifurcate.

Bifurcations occur when there is a resonance between the period of the orbit and the period of oscillations transverse to the orbit. Hence the focusing effects previously mentioned are intrinsically tied to the bifurcations of an orbit.

As mentioned earlier, mathematical analysis [15] has established the beautiful theorem that there are only five "generic" types of bifurcations. When a resonance produces a new orbit of map period m times that of the original orbit, the structure of the bifurcation is determined by the value of m, as given in Table I.

Symmetries of the system modify the structures of the bifurcations. A complete theory, listing all consequences of any possible symmetry, does not yet exist. However, for the parallel and perpendicular orbits, the consequences of the symmetry of the potential energy about $\rho=0$ and $z=0$ have been analyzed [10], and the bifurcations are modified according to the table.

Usually the closure time of a new orbit produced in an m bifurcation is m times that of its parent. However, in one case (if m is even and the map period of the parent is odd), the closure time of the new orbit is $m/2$ times the closure time of the parent. For example, the map period of the balloon orbit is 1 (odd), and its 4:1 bifurcation produces an orbit that closes at twice the closure time of the balloon.

In the following discussions the trace as a function of ε will be used to classify and show the order of the bifurcations. Additionally, the winding rates α_1, $\tilde{\alpha}_1'$, and the stability exponent are simply related to the trace by

$$\begin{aligned} &\alpha_1=\cos^{-1}[\mathrm{Tr}_1(\mathbf{z};\varepsilon)/2],\quad |\mathrm{Tr}_1|\le 2,\quad 0\le\alpha_1\le\pi \\ &\beta_1=\cosh^{-1}|[\mathrm{Tr}_1(\mathbf{z};\varepsilon)/2]|,\quad |\mathrm{Tr}_1|>2\ , \end{aligned} \tag{33}$$

$$\tilde{\alpha}_1'=\begin{cases}\alpha_1, & J_{12}>0 \\ \pi-\alpha_1, & J_{12}<0\ ,\end{cases} \tag{34}$$

TABLE I. Bifurcation type as a function of m.

m	Tr	Bifurcation type
1	2	saddle node
2	-2	period doubling
3	-1	touch and go
4	0	touch and go or four-island chain
≥ 5		five-island or m-island chain
		Bifurcations modified by symmetry
1	2	pitchfork or antipitchfork
2	-2	standard period doubling
3	-1	doubled three-island chain (symmetric period tripling)
4	0	touch and go or four-island chain
≥ 5		m-island chain (m even) or double m-island chain (m odd)

where we restrict α_1 to the principal value of the arccosine and $0 \leq \tilde{\alpha}_1' < \pi$. These winding angles are explained in Appendix D.

2. Stability, instability, and bifurcation sequences of the parallel orbit

The parallel orbit is initially stable at low energies and the trace of its Jacobian matrix is just above -2. The behavior of this trace as a function of ε is shown in Fig. 15: it has growing oscillations as ε increases towards zero.

This determines the sequence of events. At a low energy (off the diagram) is a symmetric period tripling as the trace increases through -1. Just above $\varepsilon = -0.5$ is a four-island-chain bifurcation, then a six island chain, then a pitchfork where it goes unstable; the orbit returns to stability, then as the trace decreases there is a six island chain, four island chain, doubled three-island chain, and then a period doubling where it goes unstable again. Then when it returns to stability the whole sequence is repeated.

The stability of the orbit is not visible directly in the experiment, but the associated pitchforks, period doublings, and other bifurcations produce the peaks that are the most prominent in the experiment.

3. Recurrence amplitudes for the parallel orbit

The recurrence amplitudes of the parallel orbit, C_0^a, are described by a different formula than other trajectories. The formula in our Eq. (17), Eq. (3.7a) of Ref. [3], which applies to other trajectories, gives a zero amplitude to the parallel orbit. This is incorrect since the stationary phase approximation used in Eq. (4.23a) of Ref. [3] is not applicable. The parallel orbit can be clearly seen in experiments on parallel electric and magnetic fields as well as the electric field alone case, so a better formula was needed. A proper treatment of the returning wave in the vicinity of the z axis gives a nonzero amplitude, as shown in Refs. [11,13]. The results are given in our Eqs. (3), (5), and (18).

Generally the recurrence amplitude for this orbit, $(2\pi/b)^{1/2} D_0^n(\varepsilon)$, is small [Eqs. (20) and (21) show that typically the recurrence amplitude of the parallel orbit is smaller than that of other short orbits by a factor of $\gamma^{1/6} = (B/c)^{1/6}$]. However, if we look at the experimental power spectrum at $\varepsilon = -0.45$ (Fig. 16), we can clearly see the V_1 orbit as an isolated peak at $\hat{S} = 1.05$. Also its third repetition shows up rather strongly $\hat{S} = 3.1$. Elsewhere in the experiments V_1 is hidden at the edge of the "main sequence" of orbits that bifurcate from it. In Fig. 17 we show the unsmoothed recurrence strengths as needle graphs at three different scaled energies, illustrating how V_n is usually hidden beside larger peaks. Even so, it is not completely invisible, since it combines coherently with nearby peaks. We will discuss the consequences of this later.

Figure 18 shows the recurrence amplitude versus

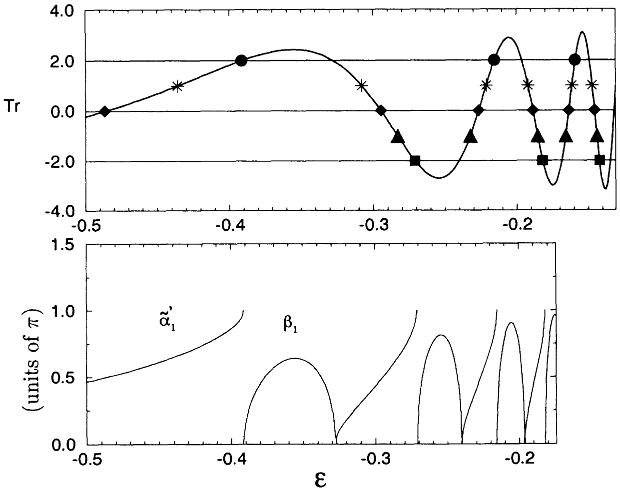

FIG. 15. The trace of the Jacobian matrix becomes increasingly oscillatory as the scaled energy approaches zero. As discussed in the text, the bifurcation behavior depends on the value of this trace. The locations of some of the bifurcations are marked. The period-doubling, 3:1, 4:1, and 6:1 bifurcations are marked with squares, triangles, diamonds, and stars, respectively. The pitchfork bifurcations creating the balloonlike orbits in the main sequence are marked by circles. The residual winding rate $\tilde{\alpha}_1'$ and the stability exponent β_1 for the parallel orbit as a function of scaled energy are also shown.

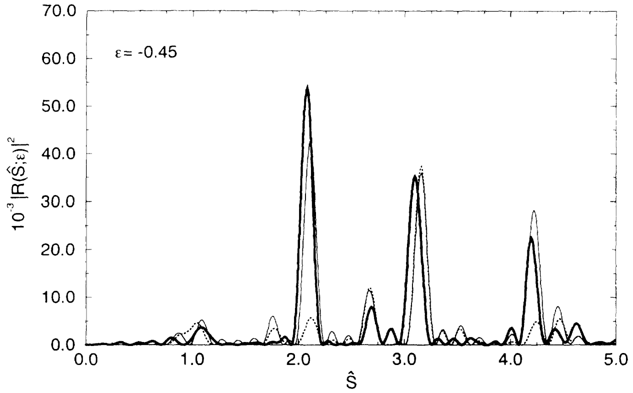

FIG. 16. The smoothed theoretical power spectrum and experimental power spectrum at $\varepsilon=-0.45$ are shown (light line and heavy line, respectively). The parallel orbit is seen in isolation as the peak at $\hat{S}=1.05$. It also contributes coherently to the peaks at $\hat{S}=2.1$, 3.15, and 4.2. If its Maslov index is not incorporated correctly, then serious discrepancy between theory and experiment arises (dashed line).

scaled energy for the first three repetitions of the parallel orbit. The picture is similar to Fig. 13, showing singularities in the recurrence amplitude at resonance points where bifurcations occur. However, in this case, the bifurcations are much richer.

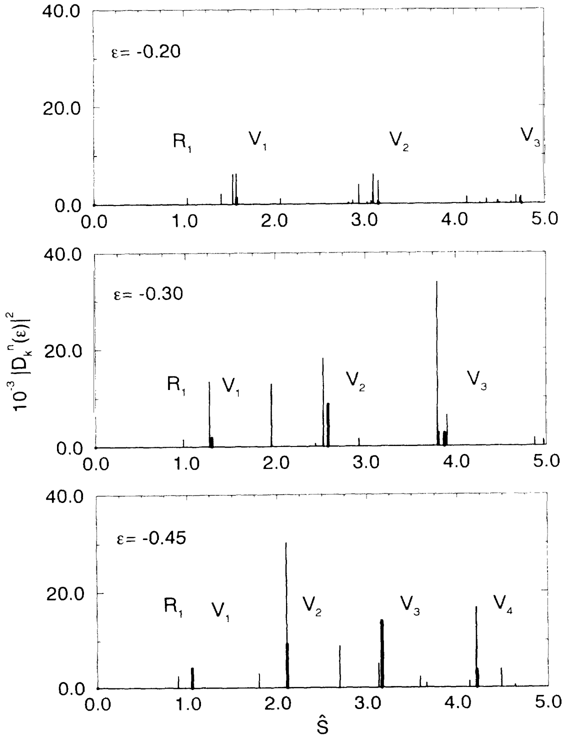

FIG. 17. The parallel orbit usually has small amplitude compared to the orbits which bifurcate from it. We show the unsmoothed theoretical recurrence strength at three different scaled energies. The parallel orbit and its repetitions are indicated by the heavy needles. At $\varepsilon=-0.45$ the first return is isolated and the subsequent returns are relatively large, combining with only a few other orbits. At the higher energies the parallel orbit becomes more and more masked by new orbits. At $\varepsilon=-0.20$ only the first return has appreciable amplitude.

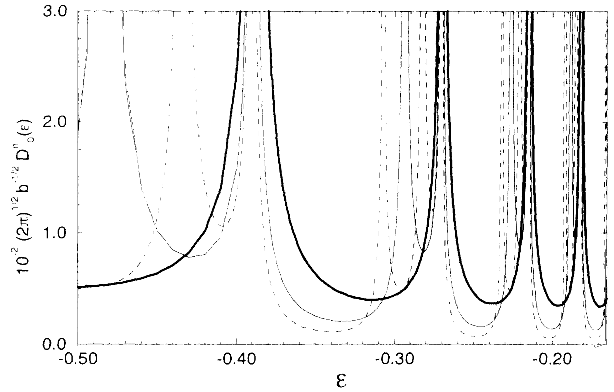

FIG. 18. The semiclassical recurrence amplitude for the parallel orbit as a function of scaled energy for $n\leq 3$ is shown. This behavior should be compared to that of the perpendicular orbit shown in Fig. 13. Each singularity occurs at a resonance where a closed orbit is produced.

4. *Maslov indices*

The experiments provide checks of the Maslov index. Like the recurrence amplitude, the Maslov index of the parallel orbit has its own formula [12]. For all other orbits we get the Maslov index by counting: $\mu_k^n=1\times$(the number of times an orbit is crossed by its neighbor) +(the number of end points on the orbit)+(the number of times the orbit intersects the z axis)$+2(n-1)$, where n is the number of returns to the nucleus. However, for V_n (a) each return to the nucleus adds only 1 to the Maslov index, not 2; (b) each time V_n is crossed by a neighbor the Maslov index increases by 2 (such a crossing implies a cylindrical focusing of waves). Therefore we have $\mu_0^n=2\times$(number of times the orbit is crossed by its neighbors)+(n for the end points at large z)+$(n-1)$ for the number of returns to the nucleus.

The Maslov index for repetitions of the parallel orbit is given in terms of $\tilde{\alpha}_1'$ by the formula

$$\mu_0^n=n\mu_0^1+2\,\mathrm{int}\left[\frac{n\tilde{\alpha}_1'}{\pi}\right]+(n-1)\ . \tag{35}$$

In contrast, the formula for many other orbits [18] is

$$\mu_k^n=n\mu_k^1+\mathrm{int}\left[\frac{n\tilde{\alpha}_1'}{\pi}\right]+2(n-1)\ . \tag{36}$$

Note the different position of the factor of 2.

For the parallel orbit, this winding angle $\tilde{\alpha}_1'$ is a piecewise smooth function of energy—it is smooth and monotonically increasing with energy when the orbit is stable, and undefined when the orbit is unstable. At the boundary points where V_1 changes from stable to unstable, $\tilde{\alpha}_1'$ is either zero or π, and $d\tilde{\alpha}_1'/d\varepsilon$ is infinite. We show its behavior and the stability exponent in Fig. 15.

The above formula for the Maslov index of the parallel orbit was tested against experiments at $\varepsilon=-0.45$. As we see from Fig. 17, the returns of the parallel orbit are relatively large and combine with the few orbits which have already bifurcated from V_n at this low energy. We have excellent agreement with experiment in Fig. 16. In contrast, before we discovered Eq. (35) we used an incorrect formula which gave poor agreement with experiment, Fig. 16 (dotted line). For example, the peak at $\hat{S}=2.1$ consists of the second repetition of the parallel orbit together with the orbit shown in Fig. 19(b)1. The latter has a Maslov index of 7, while the parallel orbit has a Maslov index of 9. The incorrect formula gave a Maslov index of 6 for the parallel orbit, and this gave a combined peak that is clearly incompatible with the measurements. In this case the experiments do not measure Maslov indices directly, but they tell us if we got them wrong.

A consequence of the relationship between bifurcations and focusing points is that the Maslov index changes at each bifurcation. In every case we find that the Maslov index of the daughter orbit in an m bifurcation is equal to the Maslov index of the mth repetition of the parent orbit just before the bifurcation.

E. Bifurcations from the parallel orbit

The most prominent features in the experimental spectrum are the fundamental, secondary, and tertiary sequences which bifurcate from V_1, V_2, and V_3. Let us look at these sequences separately.

1. *The fundamental, or main sequence*

The fundamental sequence is created at the series of 1:1 and 2:1 resonances where the V_n orbit undergoes transitions from stability to instability [10,22]. (This is in contrast to the behavior of the perpendicular orbit, which undergoes a 1:1 resonance only once and the orbits created there do not close at the origin [10].)

The first of these bifurcations occurs at $\varepsilon=-0.3913$ and it creates the B_1 orbit (here the subscript 1 is part of the name of the orbit, not the label of a repetition), which we call the "balloon." This is a "pitchfork" bifurcation, in which the parallel orbit goes from stable to unstable and two new stable orbits are produced (the balloon and its reflection through the z axis, both with map period equaling one). At this point the Maslov index of V_1 increases from 3 to 5, and the Maslov index of the balloon is 3 (consistent with the general observation mentioned above).

At $\varepsilon=-0.30$ the experimental measurements show an isolated peak at $\hat{S}=1.3$, which is the position of the B_1 orbit (Fig. 5).

As discussed earlier, the parallel orbit goes stable again near $\varepsilon=-0.32$. At this point two new unstable orbits are produced, but they do not touch the nucleus, so they are not visible in this experiment.

The next orbit in the fundamental sequence is created at the 2:1 resonance, which is the second transition from stability to instability, at $\varepsilon=-0.27099$. We classify it as a period doubling, where again the parallel orbit goes from stable to unstable but now a single orbit of twice the map period is created. It is a "snake" orbit, denoted S_1, which retraces its original path to close at the same initial angle as it started. It also is initially stable, and its initial Maslov index is 5. At this bifurcation point the Maslov index of V_1 changes from 5 to 7.

The action of S_1 is very close to that of B_1 and it is not until $\varepsilon=-0.25$ in the experiment that it is clearly visible as a separate peak near scaled action $S=1.4$.

At each scaled energy at which a 1:1 or 2:1 resonance for V_n occurs, another "balloon" or "snake" orbit is born in alternating order: $B_1, S_1, B_2, S_2, B_3, \ldots$ (these were denoted $I_1, I_2, I_3, I_4, \ldots$, respectively, in Ref. [22]). The Maslov index of the V_1 orbit increases by two upon passage through each resonance. At the limit of $\varepsilon \to -\infty$ and below $\varepsilon=-0.3913$ the Maslov index for V_1 is 3, so the Maslov index goes as $3,5,7,9,\ldots$ as the scaled energy increases towards zero. The Maslov index of each newly created orbit equals the Maslov index of the parallel orbit as it was just below the bifurcation point.

As ε increases towards zero, there is an infinite number of balloon and snake orbits. We show the first five of these in Fig. 19. Each succeeding member of this sequence has longer period than the previous member by approximately one cyclotron period. The main sequence then has simple regularities which have been discussed in

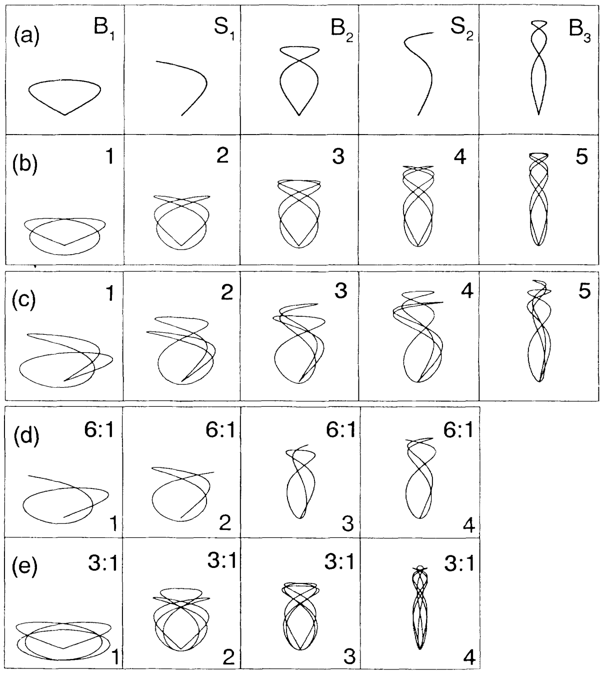

FIG. 19. (a) The first five members of the main sequence are shown in (ρ,z) coordinates. (b) In the second mountain range of peaks, the 4:1 bifurcations of the parallel orbit create a series of balloonlike orbits symmetric with respect to the z axis. (c) The second repetitions of the main sequence orbits also bifurcate to create new orbits in the second mountain range of peaks. These are 4:1 bifurcations of the balloon orbits and period doublings of the snake orbits. (d) The parallel orbit undergoes 6:1 bifurcations which are visible on the third return of that orbit for each scaled-energy range for which that orbit is stable. These bifurcations create snakelike orbits, which are self-retracing. (e) The parallel orbit also undergoes 3:1 bifurcations which are visible on the third return and these bifurcations create balloonlike orbits. The 6:1 and 3:1 bifurcations occur in alternating order as the trace alternately increases then decreases in the stability regions. The orbits created in the first four stability regions are shown in (d) and (e).

Ref. [23]. It can be treated as an almost-separable partition of motion into z oscillations and modified cyclotron oscillations (which are, however, coupled in the vicinity of the nucleus).

Figure 20 shows the main sequence as seen in the theory and experiment. As soon as each orbit in the main sequence is created, it begins its own sequence of bifurcations, with the balloons following one pattern and the snakes following another. These patterns are determined by the behavior of the trace of the Jacobian evaluated at a map period. The traces versus ε are shown for B_1 and S_1 in Fig. 21. The orbits created from these bifurcations contribute to the second and third mountain ranges seen in the experiment and will be discussed later.

2. *The secondary sequence*

The second mountain range is produced by three sets of orbits.

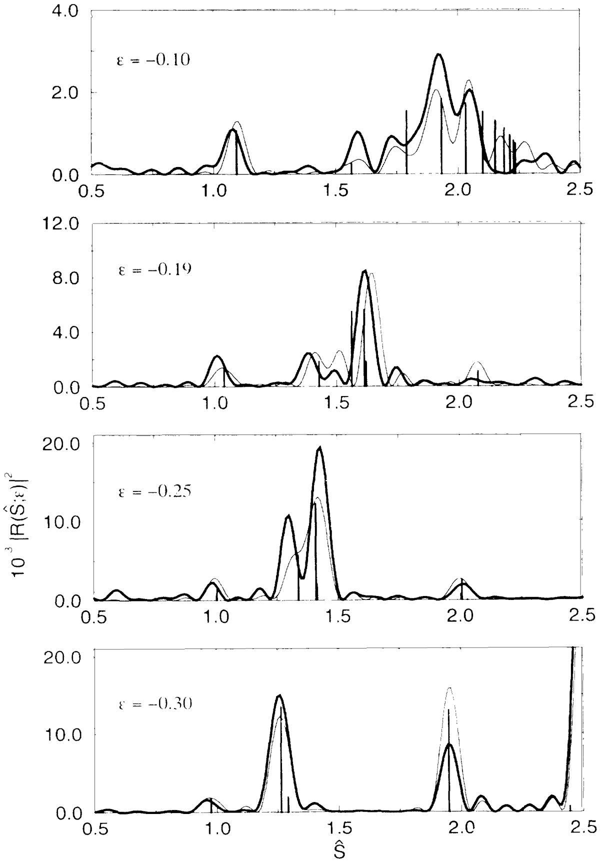

FIG. 20. The coherent sum of the oscillations due to the main sequence orbits combines to form the peaks seen in the experimental power spectrum as the first mountain range in Fig. 5. The smoothed theoretical spectrum and measured power spectrum are shown as light and heavy lines, respectively. The needles show the contributions of the individual orbits. At the lowest energy, $\varepsilon=-0.30$, only the first balloon exists, at $\varepsilon=-0.25$ the first snake is also present, at $\varepsilon=-0.19$ the second balloon, and finally at $\varepsilon=-0.10$ ten members of the main sequence exist. The agreement is quite good at each of these energies.

(a) Orbits which bifurcate from the second return of the parallel orbit. Figure 19(b) shows a family of orbits which oscillate up the z axis, come back down but miss the nucleus, and propagate up and down again before returning to the atom. Referring again to Fig. 15, one of the orbits of Fig. 19(b) is created each time the trace of the Jacobian matrix of the parallel orbit passes through zero. In the Hamiltonian bifurcation theory discussed in Ref. [10], we classify these as 4:1 bifurcations of the Poincaré half map. We see that each of the orbits is symmetric on reflection through the z axis, each is stable when created, and none of them have end points (points where the speed is zero).

The first of these bifurcations occurs at $\varepsilon=-0.4864$ and creates the orbit shown in Fig. 19(b)1. It is visible in the experimental measurement, though not in isolation, at $\varepsilon=-0.45$. We have previously seen in the discussion of Maslov indices of V_n that it combines coherently with V_2 to give the peak at $\hat{S}=2.2$.

The next bifurcation in this sequence, at $\varepsilon=-0.2946$, creates the orbit shown in Fig. 19(b)2. Each 4:1 resonance gives one new stable orbit of this type.

(b) Repetitions of main sequence orbits and their progeny. The second return of orbits in the main sequence has twice the action of the first return and these recurrences contribute to the second mountain range. Furthermore, when the main sequence orbits are stable, they also bifurcate, producing still more orbits that contribute

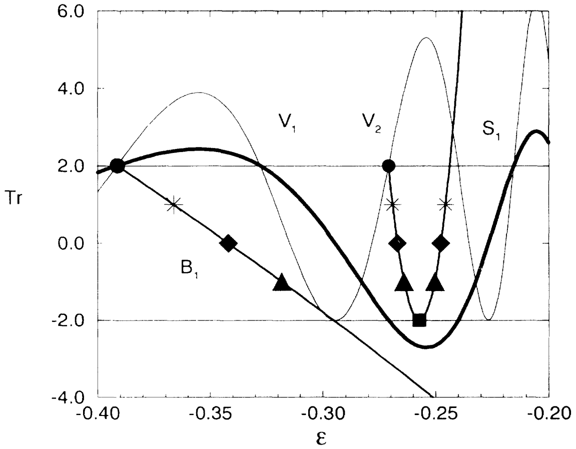

FIG. 21. The traces of the B_1 orbit and the S_1 orbit. The B_1 orbit is the first balloonlike orbit in the main sequence to be created. The trace on the first closure is also the trace on a map period. It is an almost linear function of scaled energy. The B_1 orbit undergoes 6:1, 4:1, and 3:1 bifurcations sequentially at the points indicated. This trace behavior is typical of all balloonlike orbits in the main sequence. Likewise, the S_1 orbit is the first of the snakelike orbits in the main sequence to be created. In this case, the trace on the second closure is the trace at a map period. The trace as a function of scaled energy is almost parabolic. The locations of the 6:1, 4:1, 3:1, and period-doubling bifurcation points are indicated by the stars, diamonds, triangles, and square, respectively. This trace behavior is typical for all snakelike orbits in the main sequence.

to this mountain range. The balloon orbits bifurcate on this return when their trace passes through zero. The snake orbits bifurcate as their trace touches -2.

Some orbits that bifurcate from B_1, S_1, B_2, and S_2 are shown in Fig. 19(c). They are visible in the experiments in the following sense: if they are not included, the calculated peaks do not agree with experiments. We illustrate this in Fig. 22.

(c) Exotics embedded in the secondary sequence. As mentioned earlier, some of the saddle-node bifurcations produce "exotic" orbits which themselves fall into orderly sequences. We show two such sequences in Fig. 23. It is apparent that these orbits have such an intimate connection to orbits of the main sequence that their actions must lie within the second mountain range, and their creation points must have an orderly relationship with the locations of other bifurcations.

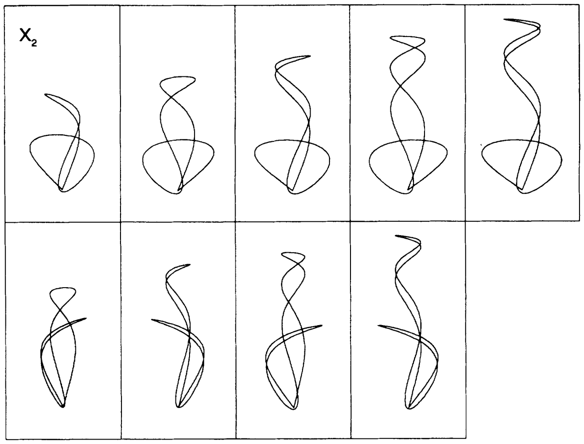

FIG. 23. Also contributing to the second mountain range, we find sequences of exotic orbits which are created in an orderly fashion. Two such sequences are shown. The first of these begins with the orbit denoted X_2 and continues with new orbits created by tangent bifurcation which are simply related to X_2. The second of these begins with an unnamed exotic and follows the same pattern. Further sets of these exotic sequences are also seen in the calculations as the energy is increased and they appear in a predictable way.

3. The tertiary sequence

Similarly, at least three families of orbits contribute to the third mountain range.

(a) Orbits which bifurcate from the third return of the parallel orbit. First we consider the bifurcations directly from V_3. Two of these orbits are created for each range of energy that the parallel orbit is stable, when the trace of the parallel orbit passes through 1 and -1, and $\tilde{\alpha}'_1=\pi/3, 2\pi/3$ respectively. These two cases are classified as six-island-chain bifurcations and symmetric-period-tripling bifurcations [10]. We show these orbits for the first four stability regions of the parallel orbit in Fig. 19(d). They are symmetric with respect to the z axis and stable at their point of creation.

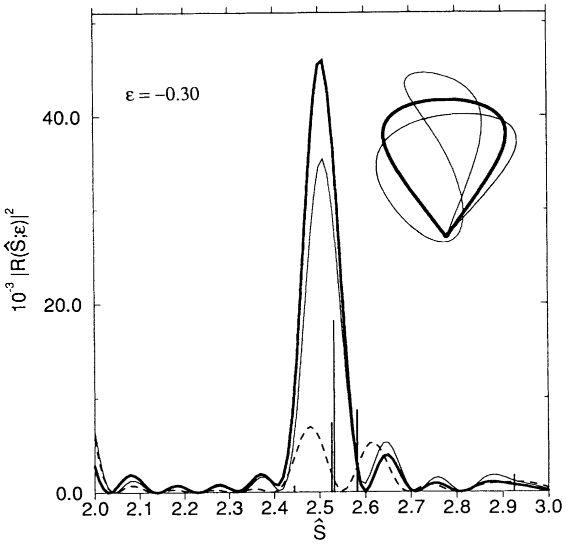

FIG. 22. The 4:1 bifurcation from the balloon [orbit (c1) in Fig. 19] produces the largest needle. It is visible in the following sense: removal of the new orbit from the closed-orbit sum ruins the agreement with the experimental measurements. The thin line and the heavy line show the theoretical and experimental recurrence spectrum, respectively, at $\varepsilon=-0.30$. The agreement is quite good. The result calculated if we remove the new orbit from the sum is shown by the dotted line. The other two needles are the second return of the B_1 orbit and of the parallel orbit, respectively, left and right of the large needle.

The first pair of these bifurcations occurs in the lowest-energy range of stability. At $\varepsilon=-0.5671$, where $\mathrm{Tr}_1=-1$, we have the 3:1 bifurcation creating a new stable orbit. This is the symmetric period tripling since $\mathrm{Tr}_1=-1$ [Fig. 19(e1)]. We see this orbit in combination with the third return of the parallel orbit in the measurements at $\varepsilon=-0.45$ (Figs. 16 and 17). The two combine coherently to produce the large peak at $\hat{S}=3.126$.

The second bifurcation in this set occurs at $\varepsilon=-0.436\,158$ and produces the orbit shown in Fig. 19(d1); it is a six-island-chain bifurcation since $\mathrm{Tr}_1=1$. As ε continues to increase, the trace for the parallel orbit passes through its first maximum and starts decreasing, so a second 6:1 bifurcation occurs at $\varepsilon=-0.307\,82$ [Fig. 19(d2)]. Recurrences associated with these orbits are masked by other large peaks.

However, the subsequent 3:1 bifurcation at $\varepsilon=-0.283\,08$ creates a stable orbit [Fig. 19(e2)] which can be seen in the experimental measurements, as a shoulder on the peak at $\hat{S}=4.0$. Figure 24 shows the theoretical spectrum calculated with and without the peak contributed by this orbit and compares both with the experiment. The agreement is quite good with the peak included.

(b) Repetitions of main sequence orbits and their progeny. Also contributing to the third mountain range are the third returns of the main sequence orbits, and orbits which are created as period-3 or period-6 bifurcations from the main sequence orbits. Let us again look at the balloon.

We showed the trace versus ε for the balloon in Fig. 21. This figure shows that the balloon undergoes a 6:1 bi-

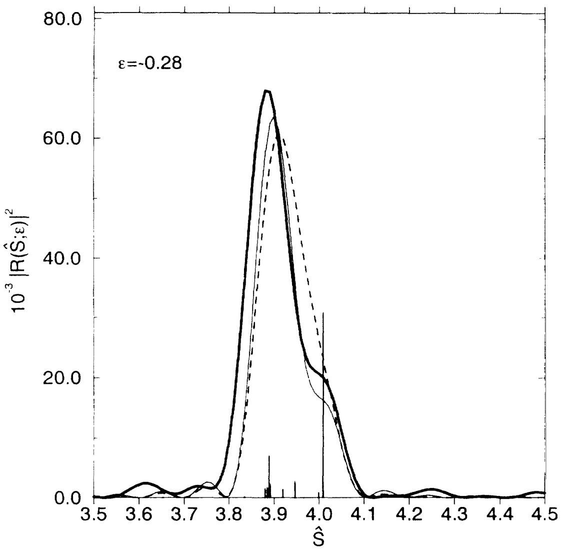

FIG. 24. As an example of the bifurcations of V_3 visible in the experiment, we show the theoretical and measured recurrence spectrum for $\varepsilon=-0.28$ as light and heavy lines, respectively. The largest needle in this figure comes from the orbit (e2) in Fig. 19 which arises from a 3:1 bifurcation of the parallel orbit. Removal of this orbit gives the theoretical result shown by the dotted line.

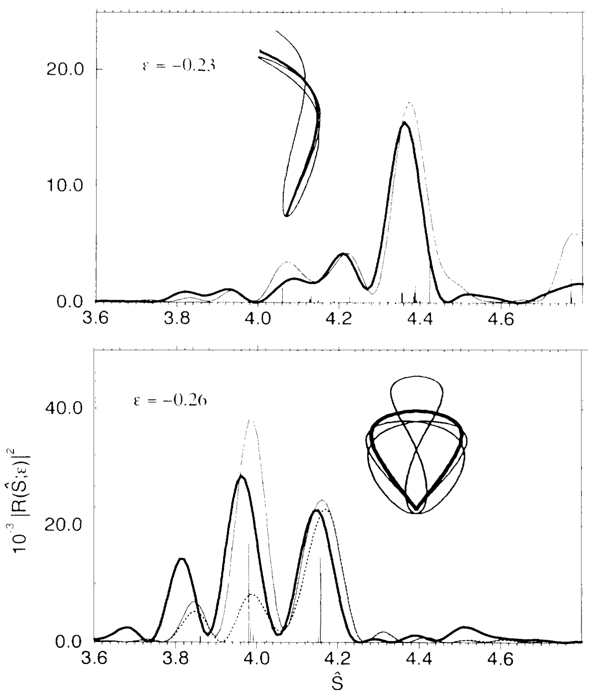

FIG. 25. The third mountain range is shown at two scaled energies. In the upper figure the main peak near $\hat{S}=4.38$ is comprised of the third return of the S_1 orbit and the coherent sum of the orbits created in its generic three-bifurcation at $\varepsilon=-0.250\,56$. One orbit created in this bifurcation is shown as an inset. The subsidiary peak near $\hat{S}=4.2$ is at the location of an exotic orbit born in the third sequence. In the lower figure, both the third return of B_1 and S_1 are seen at $\hat{S}=3.98$ and 4.16, respectively. At $\hat{S}=3.98$ the largest needle is the recurrence strength due to the unstable closed orbit, shown as an inset, which was created at the generic three-bifurcation of the balloon at $\varepsilon=-0.3161$. The smaller needles near this scaled action are the B_1 orbit and other orbits born in its 3:1 and 6:1 bifurcations. The peak at $\hat{S}=4.16$ is due to the S_1 orbit and the orbits from its nongeneric three-bifurcation, which occurred at $\varepsilon=-0.2642$.

furcation at $\varepsilon=-0.3663$, where its trace passes through $+1$, and a 3:1 bifurcation at $\varepsilon=-0.3161$, where the trace passes -1. The first is a generic six-island-chain bifurcation which creates two new unstable orbits, not particularly visible in the experiment. The second is a generic three-touch-and-go bifurcation with interesting properties that were discussed in Ref. [10]. Just below the 3:1 resonance point, a saddle-node bifurcation in the three-map creates a stable and unstable pair of closed orbits. As ε increases, the three unstable X points pass through the O point of the balloon, and then move away. The new orbits contribute to the peak at $\hat{S}=3.78$, $\varepsilon=-0.30$ (Fig. 11). Also, the new unstable closed orbit is later visible as the dominant contributor to the peak at $\hat{S}=3.98$, $\varepsilon=-0.26$ (Fig. 25).

Our calculations indicate that similar bifurcations occur on the third repetition of each balloon orbit in the main sequence.

Bifurcations of the snake orbits of the main sequence follow a different pattern. We saw in Fig. 21 that the trace for the first snake does not pass through -2, but just touches that value and turns around again. This is one symptom of a nongeneric behavior that is induced by the symmetries.

The S_1 orbit has two bifurcations on the third return, both of them being 3:1 bifurcations, where the trace passes through -1. The first of these occurs at $\varepsilon=-0.2642$, and is a new type of symmetric three-island-chain bifurcation, modified by time-reversal symmetry (Appendix C). There are actually two interleaved three-island chains, giving the appearance of a single six-island chain. The second bifurcation occurs at $\varepsilon=-0.250\,56$ and it is a generic three-bifurcation having the touch-and-go structure. Figure 25 shows the theoretical and measured recurrence strengths resulting from these bifurcations.

Our calculations indicate that all snake orbits in the main sequence also display these two bifurcations on their third repetition.

(c) Exotic orbits in the tertiary sequence. As in the second mountain range, exotic orbits contribute to some of the observed peaks in the third mountain range (Fig. 25). Again some of these exotic orbits fall into orderly patterns, comparable to the patterns suggested by Fig. 23. Others do not fit these patterns. As mentioned earlier, at present we have no global theory describing orderly sequences of saddle-node bifurcations and their associated exotic orbits.

IV. CONCLUSIONS

We have shown that this scaled-variable measurement of the absorption spectrum of hydrogen in a magnetic field gives a rich structure of recurrences. These recurrences proliferate with increasing scaled energy, consistent with the transition from orderly to chaotic classical motion of the electron.

Bifurcation theory of Hamiltonian systems gives a complete "local" description. It tells us that typical bifurcations fall into five types and that symmetries modify these structures. A certain parameter associated with a periodic orbit of a map (the trace of the Jacobian matrix as a function of energy) tells what bifurcations will occur, and in what order.

Closed-orbit theory predicts the strength of recurrences. We have good qualitative and quantitative agreement with experimental measurements, except near focal points where the semiclassical approximation to the amplitudes diverges. These points will be examined further in future studies.

ACKNOWLEDGMENTS

This work was supported by the Jeffress Foundation, the Office of Naval Research, and the National Science Foundation, through grants to the College of William and Mary and to the Institute for Theoretical Atomic and Molecular Physics. J.B.D. specially thanks the Institute for its hospitality. The work was also supported by the Deutsche Forschungsgemeinschaft.

APPENDIX A: THEORETICAL LIMITS OF THE EXPERIMENT

It is useful to examine the theoretical limits of recurrence spectroscopy. Our ability to observe and to resolve peaks associated with individual orbits in such experiments is limited by the usual resolution problems associated with Fourier transforms. The parameter a, the half range of w over which the spectrum is measured, determines the widths of the peaks in the Fourier transform. In principle, the step size in w determines the largest-action orbits that can be seen (in this experiment the step size in w was smaller than the uncertainty in w, thus, in practice, the uncertainty in w determined the visibility of long action orbits). The present experiment has an additional limitation: the laser resolution determines the longest-period orbits that can be seen.

1. Range of measurement and separation of nearby peaks in the power spectrum

The range of w along the fixed scaled-energy line in the (E,B) plane limits the ability to experimentally resolve orbits having nearly equal actions. Using the Rayleigh criterion for resolution of nearby trajectories (call them j and k), peaks in the power spectrum are just resolvable when the first minimum of the peak $\sin(ax_j)/x_j$ for the jth orbit falls at the position of the maximum of the peak $\sin(ax_k)/x_k$ for the kth orbit. This condition is $a(\hat{S}_k-\hat{S}_j)=\pi$, or

$$\hat{S}_k-\hat{S}_j \approx \frac{2\pi}{\Delta w}\ , \tag{A1}$$

where Δw is the range of w over which the spectrum is measured. When peaks overlap they combine coherently, with relative phase related to $b(\hat{S}_k-\hat{S}_j)$. Adjacent peaks may interfere constructively or destructively; this depends on the values of μ_k^n and ϕ_k for the orbits, and also upon the values of w_1 and w_2 in the experiment. Coherent sums of many peaks can be complicated, and they are very sensitive to the experimental parameters.

2. Step size of measured values and detection of large-action orbits

In an ideal scaled-variable experiment, the scaled energy ε would be precisely determined. Then if measurements were made in precise steps of size δw, Fourier transformation could give peaks up to a maximum such that

$$\hat{S}_{\max} \approx \frac{\pi}{\delta w},\quad \delta\varepsilon = 0\ . \tag{A2}$$

For example, in our case it was convenient to take steps $\delta w \approx 0.03$, so hypothetically the largest-action orbits could have actions $\hat{S} \approx 100$.

In reality the uncertainty in w was substantially larger than the convenient step size; it was governed by the precision with which we could adjust the magnet (about $\sim\frac{1}{3}\%$). Then δw in Eq. (A2) is not the step size, but the uncertainty. Therefore

$$\begin{aligned} &\delta B/B \approx 3\times 10^{-3}\ ,\\ &\delta w/w \approx 1\times 10^{-3}\ ,\\ &\delta w \approx 0.25\ ,\\ &\hat{S}_{\max} \approx 12\ . \end{aligned}$$

3. Energy resolution and detection of orbits of long period

In any real experiment, the scaled energy is determined only to the resolution allowed by the laser. In the present experiment the laser resolution also limits our ability to observe long orbits. The longest-period orbits that can be seen have $T_{\max} \approx 2\pi\hbar/\delta E$, where δE is the energy resolution of the laser.

To show this, let us express the experimental uncertainties in the photon energy of the laser, E, and the step size in the magnetic-field strength, B, as uncertainties in w and ε. These lead to an uncertainty in the phase of the sine functions in Eq. (16): writing that phase as

$$\Phi \equiv \hat{S}_k^n(\varepsilon)w\ , \tag{A3}$$

we find that small uncertainties in w and ε lead to uncertainties in Φ according to

$$\begin{aligned} \delta\Phi &= w\,\delta\hat{S}_k^n(\varepsilon) + \hat{S}_k^n\delta w\\ &= w\frac{\partial \hat{S}_k^n}{\partial\varepsilon}\delta\varepsilon + \hat{S}_k^n\delta w\\ &= w\tau_k^n\delta\varepsilon + \hat{S}_k^n\delta w\ , \end{aligned} \tag{A4}$$

where τ_k^n is the period of the orbit in units of the cyclotron time. An orbit produces visible oscillations if the combined uncertainty in Φ is less than π (Appendix B). If there were no uncertainty in w we would have

$$\tau_{\max}\approx\frac{\pi}{w\,\delta\varepsilon},\quad \delta w=0\ . \tag{A5}$$

The laser's resolution $\delta E=\sim 0.05\ \mathrm{cm}^{-1}$ gives $\delta\varepsilon=\gamma^{-2/3}\delta E\simeq 3.4\times 10^{-4}$ and $\tau_{\max}\simeq 35$ cyclotron times. Including the uncertainty in w, we have

$$\tau_{\max}\approx\frac{\pi-\hat{S}_k^n\,\delta w}{w\,\delta\varepsilon}\ , \tag{A6}$$

which (for $\hat{S}\approx 5$) gives $\tau_{\max}\approx 25$ cyclotron times.

We computed the analyzed Fourier transforms for $\hat{S}$ up to 5.0. In comparing theory with experiment, we applied a smooth cutoff factor to the theoretical recurrence amplitudes of long-period and long-action orbits. The effect is to reduce the recurrence amplitudes with increasing $\hat{S}$, and for fixed $\hat{S}$ to reduce the recurrence amplitudes for long-period orbits. The cutoff factor and its consequences are shown in Appendix B.

APPENDIX B: DERIVATION OF THE CUTOFF FUNCTION FOR ORBITS OF LONG PERIOD

Consider the oscillations arising from the nth return of the kth orbit, as described by Eqs. (16)–(18),

$$R_k^n(w;\varepsilon)=D_k^n(\varepsilon)\sin\left[\Phi_k^n(\varepsilon,w)-\frac{\pi}{2}\mu_k^n-\frac{3\pi}{4}\right],$$
$$\Phi_k^n(\varepsilon,w)=\hat{S}_k^n(\varepsilon)w\ . \tag{B1}$$

Experimental uncertainties in the photon energy and in the magnetic field produce uncertainties in ε and w, which propagate into an uncertainty in Φ according to Eq. (A4). Accordingly, the measured value is an average,

$$\begin{aligned}\overline{R_k^n}&=\frac{D_k^n(\varepsilon)}{2\delta\Phi}\int_{\Phi=\bar{\Phi}-\delta\Phi}^{\Phi=\bar{\Phi}+\delta\Phi}\sin\left[\Phi-\frac{\pi}{2}\mu_k^n-\frac{3\pi}{4}\right]d\Phi\\&=\frac{D_k^n(\varepsilon)}{2\delta\Phi}\left[\cos\left[\Phi-\frac{\pi}{2}\mu_k^n-\frac{3\pi}{4}-\delta\Phi\right]\right.\\&\qquad\left.-\cos\left[\bar{\Phi}-\frac{\pi}{2}\mu_k^n-\frac{3\pi}{4}+\delta\Phi\right]\right]\end{aligned} \tag{B2}$$

$$=D_k^n\frac{\sin(\delta\Phi)}{\delta\Phi}\sin\left[\bar{\Phi}-\frac{\pi}{2}\mu_k^n-\frac{3\pi}{4}\right]\ . \tag{B3}$$

Thus we have the original amplitude diminished by a $\sin(\delta\Phi)/\delta\Phi$ "cutoff" function, with $\delta\Phi(w;\varepsilon)$ given by Eq. (A4). The effect of the cutoff function on the theoretical spectrum at $\varepsilon=0.0$ is shown in Fig. 26.

The relationship between the periods and the scaled actions for orbits in the main sequence is worth noting in connection to this cutoff. Successive members of the main sequence stretch farther and farther out the z axis, so their periods become very long, especially as ε increases toward zero. However, their actions do not increase so rapidly, so many of them remain well within the action range discussed in this paper ($\hat{S}\leq 5$). The effect of the laser bandwidth, however, reduces the peaks associated with these long-period orbits. Thus there is only a finite number of orbits in the main sequence which need to be considered in the closed-orbit sum, even at $\varepsilon=0$.

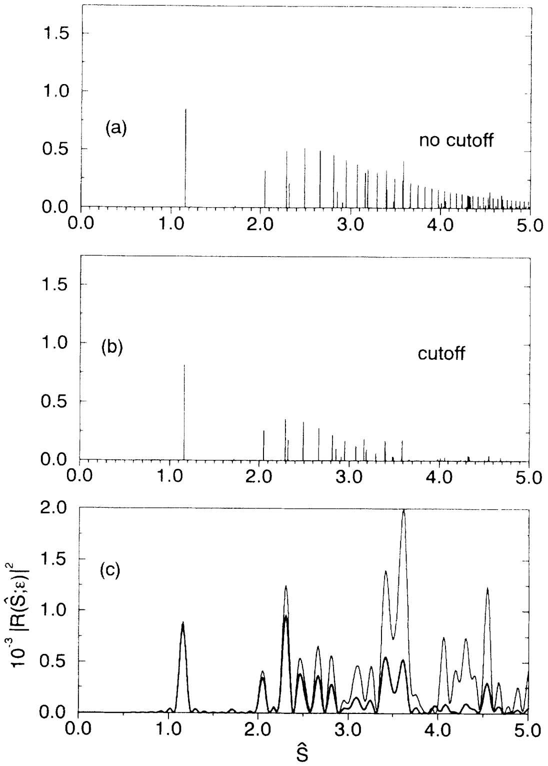

FIG. 26. The effect of the cutoff on the theoretical recurrence strength at $\varepsilon=0.0$ is shown: the heavy line is the theory with the cutoff and the thin line is the theory without the cutoff.

APPENDIX C: TIME-REVERSAL SYMMETRY AND THREE-BIFURCATIONS OF SNAKELIKE ORBITS

The trace of the Jacobian matrix for the snakelike orbits passes through -1 twice. Therefore these orbits have two bifurcations which are 3:1, yet we observe that these two bifurcations are quite different in character. The resolution to this puzzle is found in the time-reversal symmetry of the system.

To understand it, we must distinguish between orbits in configuration space and orbits in phase space. In configuration space, if the Hamiltonian is purely quadratic in the momenta, an orbit and its time reverse always coincide. On the other hand, in phase space the time reverse of an orbit is in most cases a path which is completely distinct from the original orbit. Only if the orbit is self-retracing in configuration space does the time reverse in phase space lie upon the original orbit.

Suppose we are given a self-retracing orbit (a "snake"), and suppose that at some point that orbit has a bifurcation. The newly created orbit might or might not be self-retracing. If it is not self-retracing, then the time-reversal symmetry insists that there must be another orbit, distinct in phase space, which is the time reverse of that new orbit. Therefore the bifurcation is forced to create not one new orbit but two. In this way, the bifurcation is nongeneric. We find that some of the bifurcations of the snake orbits have their structures modified as a result of this symmetry.

How does this behavior manifest itself in the three-bifurcations of the S_1 orbit? The higher-energy 3:1 bifurcation at $\varepsilon=-0.250\,56$ is a generic three-bifurcation. It turns out that the new orbits bifurcating from S_1 at this energy are self-retracing and therefore automatically satisfy the time-reversal symmetry. This symmetry gives "nothing new," and the bifurcation has the same touch-and-go structure as the three-bifurcation of the balloon. (A saddle-node bifurcation creates the new period-3 orbit, which then collides with the balloon and passes through it; see Fig. 14 of Ref. [10].)

In contrast, the lower-energy 3:1 bifurcation at $\varepsilon=-0.2642$ is nongeneric, and something different does happen there. The new orbit bifurcating from S_1 is not self-retracing, so the symmetry requires the creation of another closed orbit from S_1. The symmetry forces the creation of two interleaved three-island chains. The surface of section looks like a six-island chain surrounding S_1.

Let us look at this another way, examining the winding rates on the Poincaré half-map and the full map. The "half-map" is the function $\mathbf{z}=f(\mathbf{z}_0;\varepsilon)$ as in Eq. (30), but evaluated at the first closure of the S_1 orbit, not at the map-period which occurs on the second closure. We denote by $\mathrm{Tr}_{1/2}$ the trace of the Jacobian matrix of this map evaluated at the closed orbit. Tr_1 is the trace of the corresponding Jacobian matrix at the map-period of the orbit. The rotation angles for these two maps are denoted $\alpha_{1/2}$ and α_1.

On the half map the trace of S_1 starts at -2 and increases, passing through -1, 0, 1, and 2 almost linearly. If $\mathrm{Tr}_{1/2}=-1$ then $\alpha_{1/2}=\pm\pi/3$, but the trace evaluated at a period, Tr_1, also equals -1, and therefore $\alpha_1=\pm 2\pi/3$. The points on the half map and the points on the full map both rotate by $\pi/3$ on each iteration but in opposite directions. The result is shown in Fig. 27 as the set of open circles surrounding S_1. We have three fixed points in both the upper and the lower (p_v,v) plane forming triangles with the same orientation. The operation of time reversal is equivalent to reflection on the surface of section through the $p_v=0$ axis. If we do this, a new orbit is seen which forms triangles in both the upper and lower (p_v,v) plane with the opposite orientation from those of the first orbit.

When $\mathrm{Tr}_{1/2}=1$, then $\alpha_{1/2}=\pm\pi/6$, but now the trace evaluated at the period $\mathrm{Tr}_1=-1$ and $\alpha_1=\pm\pi/3$. The points on the half map rotate by $\pi/6$ for each iteration, while those of the full map rotate $\pi/3$ for each iteration, and both rotate in the same direction this time. The result is shown in Fig. 28, where we have three fixed points on both the upper and lower (p_v,v) plane, but now the reflection through the $p_v=0$ axis simply maps the upper triangle of points into the lower triangle. No new closed orbits are needed to satisfy the constraint of time-reversal symmetry.

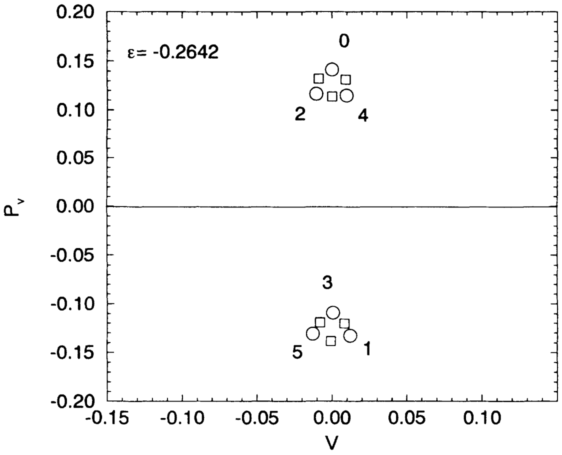

FIG. 27. The symmetry-modified three-bifurcation of the snake has two interleaved sets of unstable fixed points on the Poincaré half-map. A more detailed picture would look like Fig. 8 of Ref. [10]. If we start on the fixed point with p_v positive and greater than p_v of the snake (circular symbol), we get the upright triangles in both the upper and lower half-planes. If we start on the fixed point with p_v positive and less than that of the snake (square symbol), we get the inverted triangles in the upper and lower half-planes. The numbers 0–5 show the order in which the trajectory winds about S_1 with 6 bringing it back to the original point, 0.

We may reemphasize that since the "additional" orbit that arises in the nongeneric bifurcation is the time reverse of its partner, the two coincide in configuration space. Nevertheless, they are distinct in phase space, and this produces the unusual structure of the bifurcation.

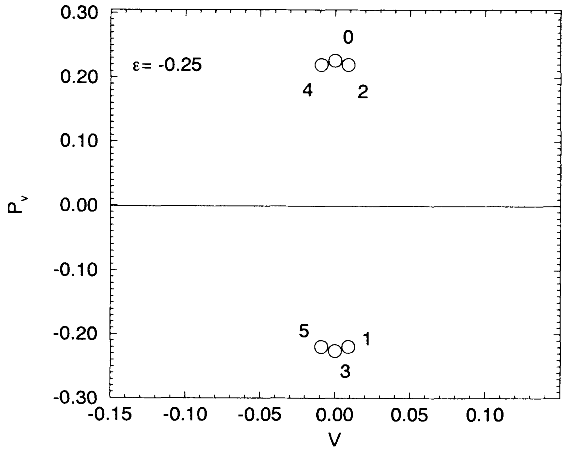

FIG. 28. The generic three-bifurcation (we only show the unstable member for simplicity) gives one set of triangles on the Poincaré half map. A more detailed picture would look like Fig. 14 of Ref. [10]. If we start on the fixed point with positive p_v, we reach all other fixed points as we follow the trajectory. The numbers 0–5 show the order in which the trajectory winds about S_1 with 6 bringing it back to the original point, 0. The trajectory is its own time reversal.

APPENDIX D: WINDING ANGLES AND MASLOV INDICES

The winding angles in Eqs. (33) and (34) have the following meaning for the parallel orbit. Suppose we integrate the equations of motion for the parallel orbit $[u(\tau),p_u(\tau),v(\tau)=0,p_v(\tau)=0]$, and simultaneously integrate equations of motion for a linearized neighbor of the parallel orbit, $[u(\tau),p_u(\tau),\delta v(\tau),\delta p_v(\tau)]$, having initial conditions $u(0)=0,\delta v(0)=0,\delta p_v(0)=(\text{small})$. We monitor $\delta v(\tau)$ and $\delta p_v(\tau)$ up to the first return of the parallel orbit at time T_1. These two variables define a phase-space point that moves in a curve around the origin. If the variables $[\delta v(T_1),\delta p_v(T_1)]$ are appropriately scaled to a normal form [12], then $\alpha(T_1)$ represents the total angle swept out by the phase point up to the first return. The residual winding angle $\tilde{\alpha}_1'$ given in Eq. (34) is defined as this full winding angle at the first closure modπ:

$$\tilde{\alpha}_1'=\alpha_1(T_1),\quad \text{mod}\pi \; . \tag{D1}$$

We have the following consequences.

(1) The number of times the neighbor crosses the parallel orbit before the first closure is $\text{int}[\alpha_1(T_1)/\pi]$.

(2) The Maslov index of the returning wave at first closure is twice this number of crossings plus one for the end point:

$$\mu_0^1=1+2\,\text{int}[\alpha_1(T_1)/\pi] \; . \tag{D2}$$

(3) The full winding angle $\alpha_1(T_1)$ can be obtained from the residual winding angle $\tilde{\alpha}_1'$ using the formula

$$\alpha_1=\tfrac{1}{2}(\mu_0^1-1)\pi+\tilde{\alpha}_1' \; . \tag{D3}$$

(4) The full winding angle at the nth return is n times the winding angle at the first return,

$$\alpha_1(nT_1)=n\alpha_1(T_1) \tag{D4}$$

and the number of times the neighbor crosses the parallel orbit is $\text{int}[n\alpha_1(T_1)/\pi]$.

(5) Therefore the Maslov index on the nth return is

$$\begin{aligned}\mu_0^n&=n+(n-1)+2\,\text{int}\left[\frac{n\alpha_1(T_1)}{\pi}\right]\\ &=n+(n-1)+2\,\text{int}\left\{n\left[\frac{\frac{1}{2}(\mu_0^1-1)\pi+\tilde{\alpha}_1'}{\pi}\right]\right\}\\ &=n\mu_0^1+2\,\text{int}\left[\frac{n\tilde{\alpha}_1'}{\pi}\right]+(n-1) \; .\end{aligned} \tag{D5}$$

---

[1] W. R. S. Garton and F. S. Tomkins, Astrophys. J. **158**, 839 (1969); K. T. Lu, F. S. Tomkins, and W. R. S. Garton, Proc. R. Soc. London, Ser. A **362**, 421 (1978); A. R. Edmonds, J. Phys. (Paris) Colloq. **31**, C4-71 (1970).

[2] J. Main, G. Wiebusch, A. Holle, and K. H. Welge, Phys. Rev. Lett. **57**, 2789 (1986).

[3] M. L. Du and J. B. Delos, Phys. Rev. Lett. **58**, 1731 (1987); Phys. Rev. A **38**, 1896 (1988); **38**, 1913 (1988).

[4] D. Wintgen, Phys. Rev. Lett. **58**, 1589 (1987); D. Wintgen and H. Friedrich, Phys. Rev. A **36**, 131 (1987); M. C. Gutzwiller, J. Math. Phys. **8**, 1979 (1967); **10**, 1004 (1969); **11**, 1791 (1970); **12**, 343 (1971).

[5] B. R. Johnson and J. L. Kinsey, J. Chem. Phys. **91**, 7638 (1989).

[6] A. Carrington and R. A. Kennedy, J. Chem. Phys. **81**, 91 (1984).

[7] J. P. Pique, Phys. Rev. Lett. **58**, 475 (1987).

[8] E. J. Heller (private communication).

[9] A. Holle, J. Main, G. Wiebusch, H. Rottke, and K. H. Welge, Phys. Rev. Lett. **61**, 161 (1988).

[10] J.-M. Mao and J. B. Delos, Phys. Rev. A **45**, 1746 (1992).

[11] J. Gao and J. B. Delos, Phys. Rev. A **46**, 1449 (1992); **46**, 1455 (1992).

[12] J.-M. Mao, J. Shaw, and J. B. Delos, J. Stat. Phys. **68**, 51 (1992).

[13] E. B. Bogomolnyi, Zh. Eksp. Teor. Fiz. **96**, 487 (1989) [Sov. Phys. JETP **69**, 275 (1989)]; Pis'ma Zh. Eksp. Teor. Fiz. **47**, 445 (1988) [JETP Lett. **47**, 526 (1988)].

[14] J. B. Delos, S. K. Knudson, and D. W. Noid, Phys. Rev. A **28**, 7 (1983).

[15] K. R. Meyer, Trans. Am. Math. Soc. **149**, 95 (1970); M. A. M. Aguiar, C. P. Malta, M. Baranger, and K. T. R. Davies, Ann. Phys. (N.Y.) **180**, 167 (1987).

[16] In a Hamiltonian system, the technical name for a saddle-node bifurcation is "saddle-center" bifurcation, or "tangent bifurcation." Let us also note that each member of the stable-unstable pair of exotic orbits in Fig. 7 has a time-reversed partner which is reflected so that it is outgoing in the first quadrant. Each orbit and its time-reversed-and-reflected partner gives separate but equal contributions to the sum in Eq. (2). When we plot needle graphs we combine the recurrence amplitudes of such partners.

[17] The singular behavior in Fig. 8 reminds us of the singularity in the WKB approximation at a turning point. The quantum wave function gets large, but remains finite, and it spills over slightly into the classically forbidden region.

[18] Equations (27), (28), and (36) apply to orbits called "type 1" in Ref. [12]. They do not necessarily apply to "type-2" orbits.

[19] The resonance is denoted 4:1 to conform with the classification of the resonance on the Poincaré surface of section given in Ref. [10]. We will in general follow this standard.

[20] The oscillator-strength density is related to the matrix element $\langle D\phi_i|G_E|D\phi_i\rangle$. Part of $G_E|D\phi_i\rangle$ is the returning wave, and we are looking at its overlap with the initial state $\langle D\phi_i|$.

[21] There is no universal convention on the matrix representing the derivative of the Poincaré map, $J_1=\partial(q_1,p_1)/\partial(q,p)$. In fact, Refs. [10,12] use two different naming conventions for the matrix elements. We will follow the convention of Ref. [12].

[22] H. Friedrich and D. Wintgen, Phys. Rep. **183**, 37 (1989).

[23] J. Main, A. Holle, G. Wiebusch, and K. H. Welge, Z. Phys. D **6**, 295 (1987).